



MATTHIAS WAHRBICHLER, BSC

Modelling, simulation and control of a flow heater

Master Thesis

to achieve the university degree of

Diplom-Ingenieur

Master's degree programme: Electrical Engineering and Business

submitted to

Graz, University of Technology

Supervisor

Assoc.Prof. Dipl-Ing. Dr.techn. Markus Reichhartinger

Co-supervisor

Dr.techn. Stefan Koch, BSc MSc

Institute of Automation and Control

Head: Univ.-Prof. Dipl-Ing. Dr.techn. Martin Horn

Graz, October 2020

Affidavit

I declare that I have authored this thesis independently, that I have not used other than the declared sources/resources, and that I have explicitly indicated all material which has been quoted either literally or by content from the sources used. The text document uploaded to TUGRAZonline is identical to the present master's thesis.

Date

Signature

Abstract

This thesis describes the control-loop design for a flow-heater used for process silicon wafers in the semiconductor industry. Increased demands due to technological processes require a more precise control-loop for wafer spin-clean-systems. The approach proposed in this thesis is to take a mathematical model of the plant, which describes the heat flow of the heater. Two control algorithms based on the model are tested on a test rig. The first control algorithm is a state controller, the second is a model-predictive controller. The computation-intensive MPC control algorithm also can consider restrictions on the output temperature. Experiments have shown that both controllers are suitable. However, the model predictive controller has a shorter settling time and smaller temperature fluctuations.

Kurzfassung

Diese Masterarbeit stellt einen modellbasierten Reglerentwurf für einen Durchlauferhitzer, der für die Wafer-Reinigung in der Halbleiterindustrie eingesetzt wird, vor. Der technologische Fortschritt der Halbleiterindustrie erfordert auch die genauere Temperaturregelung von Prozessflüssigkeiten, die Wafer-Reinigungs-Maschinen eingesetzt werden. Der Ansatz ist, ein mathematisches Modell des Durchlauferhitzers zu entwickeln, welches die Wärmeverteilung im Durchlauferhitzer beschreibt. Es werden zwei verschiedene Regelalgorithmen vorgestellt, beide werden am Teststand experimentell erprobt. Der erste Algorithmus ist ein Zustandsregler, der zweite Regler ist ein Model-Prädiktiver-Regler. Dieser rechenintensive Algorithmus kann auch Beschränkungen der Ausgangsgröße berücksichtigen. Beide Regelalgorithmen funktionieren am Teststand. Der modelprädiktive Regler zeigt bei den durchgeführten Versuchen jedoch kürzere Einschwingzeiten und kleinere Abweichungen von der gewünschten Temperatur.

Contents

Abstract	iii
1. Introduction	1
1.1. Semiconductor chips	1
1.2. Problem definition	3
2. Test rig	7
2.1. Description of the main components	10
2.1.1. Flow heater	10
2.1.2. Programmable Logic Controller (PLC)	13
2.1.3. PT100 Temperature sensors	13
2.2. Test rig usage	14
3. Mathematical modelling	15
3.1. The one-dimensional heat equation	15
3.2. Model with the heating cartridge as heat source	17
3.2.1. Temporal discretization	20
3.2.2. Parameter identification	20
3.3. Model with indefinite small heat source	23
3.4. Validation and comparison of models	25
4. Disturbance observer-based linear state feedback controller	29
4.1. Luenberger observer	29
4.2. Design of the state feedback controller	31
4.3. Experimental validation	34
5. Model predictive control	37
5.1. Model predictive control without considering constraints	40
5.2. Model predictive control with constraints	41
5.2.1. Theory	41
5.2.2. Simulation results	45
5.2.3. Experimental results	51
5.3. Results and Comparison	52
6. Conclusion	55

Contents

Bibliography	57
A. Table of material properties and Equations	59
B. Schematic	63

List of Figures

1.1.	Integrated circuits on a circuit board.	2
1.2.	Silicon wafer.	2
1.3.	Wafer spin-clean system.	3
1.4.	Collapse bend	3
1.5.	Collapse break [10]	3
1.6.	Sketch of a wafer pattern	4
1.7.	PI-Controller step response	5
1.8.	Transport delay at flow = 500 ml/min	5
2.1.	Test rig with its components	8
2.2.	Test rig front side with water supply	8
2.3.	Test rig control box	8
2.4.	Test rig flow plan	9
2.5.	The flow heater	10
2.6.	Heater characteristic curve at 400 V supply	12
2.7.	Automation Studio Target for Simulink.	14
3.1.	Cross-sectional view of the heater	16
3.2.	Top view of the heater with marked boundary conditions.	18
3.3.	Measured data for optimization	22
3.4.	Example of recorded data	22
3.5.	Comparison of two formulas for the heat transfer coefficient	24
3.6.	Different input conditions for validating the Models	26
3.7.	Validation and comparison of the Models	26
4.1.	Block diagram of the control-loop status controller	33
4.2.	Test results using the proposed controller obtained from the test rig.	34
4.3.	State feedback controller - comparison of quantisation steps	35
5.1.	Block diagram of MPC	40
5.2.	Time diagrams from an experiment of MPC without constraints on the test rig.	41
5.3.	Block diagram of the MPC-Controller	44
5.4.	Simulation with constraints to the actuating variable and $T_d = 5s$	45
5.5.	Simulation with constraints, qpooases algorithm with $T_d = 1s$	46

List of Figures

5.6. Simulation with constraints qpooases algorithm with $N_p = 50$ and $T_d = 1s$	47
5.7. Simulation with constraints Hildereth-algorithm with $T_d = 1s$	48
5.8. Simulation with constraints, comparison of algorithms with $T_d = 1s$	49
5.9. Simulation with constraints, comparison of algorithms with $T_d = 1s$, zoomed view	49
5.10. Simulation with constraints and disturbance.	50
5.11. Simulation with constraints and disturbance, zoomed view.	51
5.12. MPC with constraints on the test rig. Difference = $0.1\text{ }^\circ\text{C}$	52
5.13. MPC with constraints on the test rig. Difference = $0.4\text{ }^\circ\text{C}$	53
5.14. MPC with constraints on the test rig. Difference = $0.5\text{ }^\circ\text{C}$	54
5.15. Comparison: MPC vs. Status controller	54

1. Introduction

The focus of this master thesis is on the heater for the rinsing liquid for one of the most important steps in the semiconductor manufacturing process: the wafer cleaning after etching.

1.1. Semiconductor chips

The core elements of almost all modern electronic devices are integrated circuits, which are called microchips or "chips", see Figure 1.1. Integrated circuits are built on a semiconductor substrate, also called wafer. A wafer is shown in Figure 1.2. Semiconductors are materials that have an electrical conductivity, which is between a conductor and an isolator. The semiconductor base material often is silicon, which is doped for different conduction properties. Doping is the targeted contamination of semiconductor base material to get conductor material with positive or negative charge carriers.

By setting positive- and negative doped materials together, diodes and transistors are built out of it. The first point-contact transistor was developed in the year 1947. Approximately ten years later, the first integrated circuit consisting of a few transistors, was built. Research and development in that field led to a steadily increasing number of transistors per area: "The number of transistors in integrated circuits doubles every two years, since the 1960s", this is stated by the well-known Moore's Law. Today's integrated circuits often consist out more than 12 billion transistors. The latest technology are transistors with a gate width of only 14 nanometres ($14 \cdot 10^{-9}$ m).

Integrated circuits are produced in semiconductor fabrication plants (FAB). The central part of a fab is the cleanroom where the production facilities for the various production steps are located. Figure 1.3 shows a semiconductor process machine. Semiconductor chips are built on silicon wafers. A common wafer-diameter is 300 mm. The wafer fabrication requires several process steps: ion implantation, striping, deposition, photoresist coating, exposure, developing, etching, and cleaning which are carried out repeatedly.

Lam Research (company, Headquarters: Fremont, California, US), the research partner of this project, is a leading manufacturer for semiconductor-process-equipment.

1. Introduction

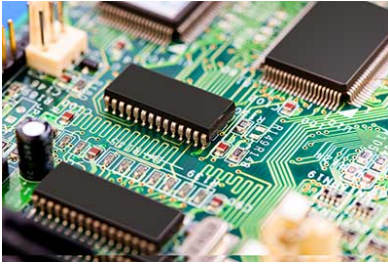


Figure 1.1.: Integrated circuits on a circuit board.

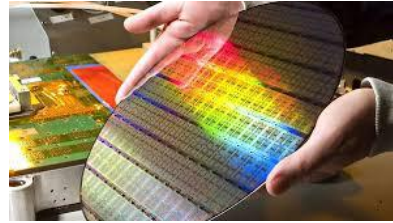


Figure 1.2.: Silicon wafer.

One product-group, which is developed at their site in Villach, are so-called single wafer spin-clean-systems. These machines operate with a dispenser arm, which applies rinsing liquid onto the rotating wafer. The flow heater, which is under consideration in this thesis, is used for heating the rinsing liquid in spin-clean-systems.

As previously mentioned, the technological process of the semiconductor industry (Moore's law) leads to more and more transistors per area. However, the structures are not only getting smaller but also higher. This issue leads to the risk of the so-called pattern collapse during the cleaning process. The pattern collapse is basically caused by the capillary forces of the rinse liquid and other factors.

"The factors which affect pattern collapse can be categorized into three groups: (i) pattern's geometry, (ii) rinse liquid and its related capillary forces, and (iii) pattern's material", [1].

The collapse can be classified into two modes: "deformation" and "peeling". Figure 1.4 shows a deformation-bend from scanning electron microscope. A deformation break is shown in Figure 1.5.

"Laplace pressure in case of pattern collapse is the pressure difference across the liquid-air interface and is a function of rinse liquid surface tension and rinse interface curvature. The surface tension force increases by increasing the contact angle θ , pattern height H to width w ratio, and trough d to width ratio, see Figure 1.6", [1].

The surface tension in liquids depends on the temperature. "In general, the surface tension decreases when the temperature increases" [11]. Thus, one solution to prevent pattern collapses is to increase the temperature of the rinsing liquid. Another approach is to replace the water, which is usually used for cleaning, by liquids with substantially convex surface tension such as isopropanol (IPA). For heating the liquid, a flow heater is installed in the spin-clean-systems. Additionally, the rotating wafer is also heated with LEDs from the bottom side to compensate the heat losses, see [6].

To ensure a constant fluid temperature during the process, a control loop is used.



Figure 1.3.: Wafer spin-clean system.

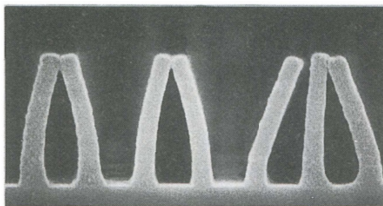


Figure 1.4.: Collapse bend

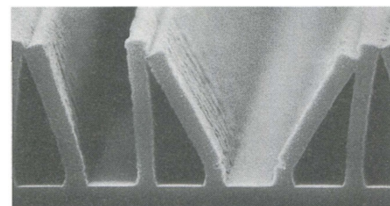


Figure 1.5.: Collapse break [10]

This thesis deals with the controller design for the flow heater. Two other control concepts are described: A "Model-based state feedback Controller" and a "Model Predictive Controller".

1.2. Problem definition

The control goal is to heat up the used liquid to a desired temperature and maintain this temperature during processing. For this purpose, the existing flow heater should be used. Currently, a PI-Controller is used. PI-Controllers are the most commonly used control-algorithms in industry. Flow heaters (and heaters in general) are plants with dead time, making the control challenging. Often the

1. Introduction

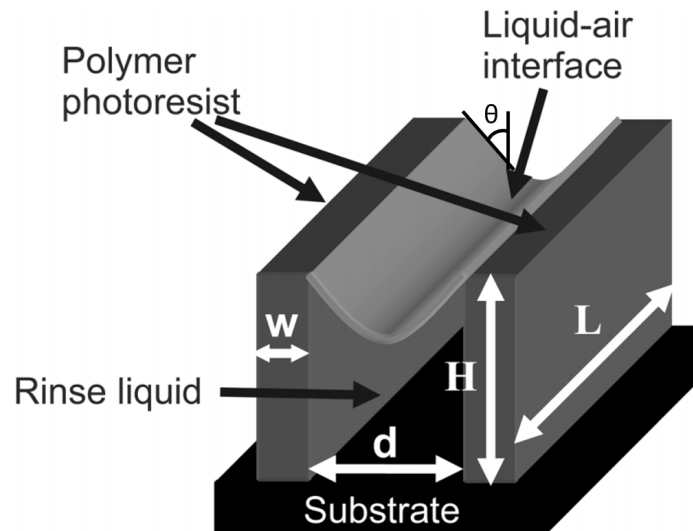


Figure 1.6.: Sketch of a wafer pattern

PI-Controllers at plants with dead-time cause overshooting. When the overshoot exceeds the boiling point of the fluid, bubbles appear. The bubbles of boiling isopropanol disturb the process. Boiling isopropanol represents a hazard due to its flammability. Thus, the aim is to design a control loop without overshoot.

The specifications are a temperature range between 20 - 80 °C. Common setpoints are: 41.5 °C and 78 °C. The upper limit (absolute maximum) the fluid is allowed to get is the boiling point of isopropanol i.e. 82,5 °C.

Figure 1.7 shows a simulated step response of the PI-controller where the overshoot in the output variable becomes evident. The overshoot may be caused by two mechanisms: One is the transport-delay of the plant, and the second is the wind-up-effect.

The plot in Figure 1.8 shows the heater response at nominal flow when changing the actuating variable abruptly from 0 to 100 % or from 100 to 0 %. It can be seen that the heater has a delay, which means that the measured output still gets warmer even if the heater is already switched off. The measured delay time on the real hardware was 18 to 20 seconds at nominal flow ($500 \frac{ml}{min}$).

For the controller design, the following issues need to be taken into account: As already mentioned, the isopropanol must never exceed the boiling point: It is a hazardous liquid, flammable at the boiling point. When measuring the fluid temperature at one specific point, make sure that the measuring point has the highest fluid temperature. In addition, the heater is divided into four streams, so that at least four temperature sensors would be required to measure the liquid

1.2. Problem definition

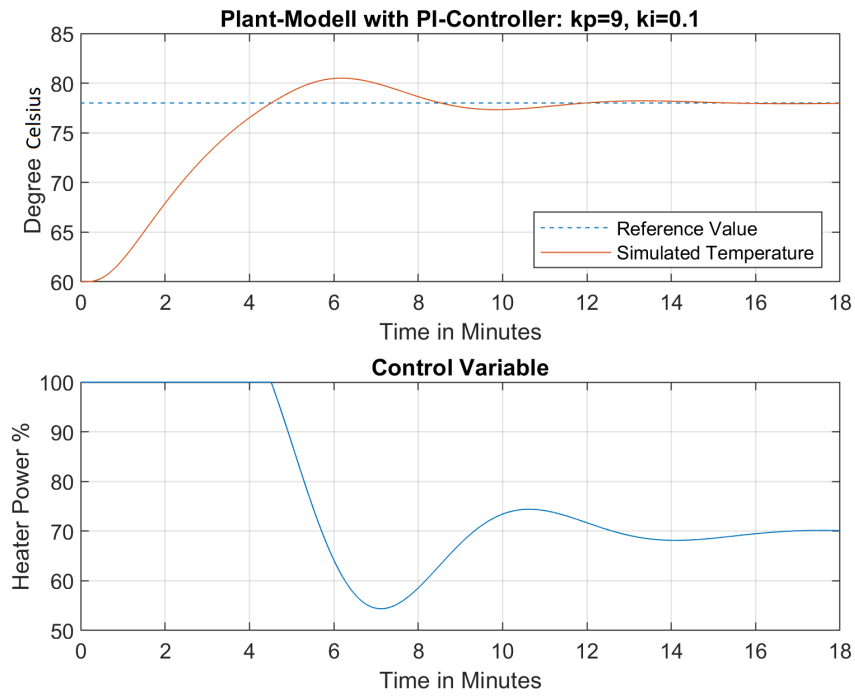


Figure 1.7.: PI-Controller step response

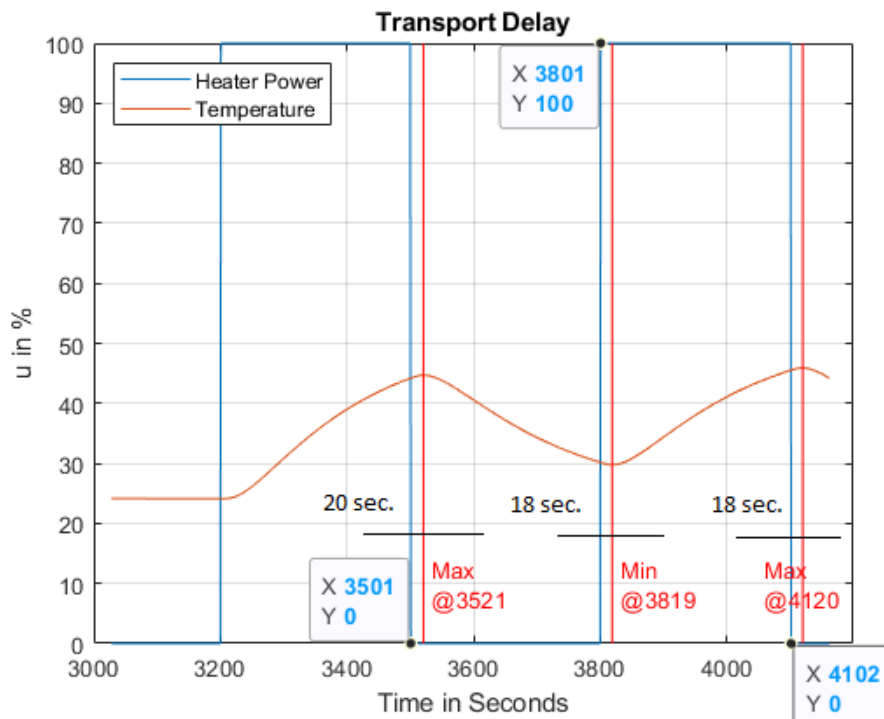


Figure 1.8.: Transport delay at flow = 500 ml/min

1. Introduction

temperature. Furthermore, the fluid temperature cannot be measured well because it is conducted in perfluoroalkoxy (PFA) tubes. It is not allowed to change a tube segment to any other material. PFA is a thermoplastic resin with the correct chemical and mechanical properties for being used at this application in a FAB.

Basically, there are two different types of temperature sensors for PFA Tubes: The first one is a sensor that is mounted in a fitting and protrudes into the tube. At the point where the sensor protrudes into the tube, the cross-section is reduced, and a pressure difference occurs. When the fluid temperature is near the boiling point, the pressure difference might lead to boiling fluid. The second type are temperature sensors which are clamped on the PFA-tube. Such sensors have a slow response time (5 - 10 seconds), and therefore it is not reasonable to use them in the control loop.

In the heater, there are already two temperature sensors of type PT100 built-in, located between the metal body and the tubes. One of them is used for safety shut-off, and the second is used for the control-loop. The advantage is that these temperature sensors have a short response time, this variant is cost-effective, and only one temperature sensor is used for all four streams. The disadvantage is that the real fluid temperature is lower than the reference value, because the heat transfer through the pipe wall is not considered. An important requirement is a repeatability concerning the temperature since every wafer must be processed at the same temperature.

2. Test rig

The test rig is used for parameter identification and controller tests in the laboratory. An existing test rig from a related master thesis was modified for this project. The related master thesis is "Design of a Model-based Liquid Flow Controller" from Martin Kleindienst [4]. For this work, several extensions and modifications of the test rig were necessary. The modification included the installation of the heater with solid-state relays, installation of new temperature sensors as well as commissioning of the PLC. The modified test rig is shown in Figure 2.1 with its components in Figure 2.2, where the front side is pictured with the water supply and in Figure 2.3 which shows the control box. The corresponding liquid flow plan is pictured in Figure 2.4. The electrical schematic is provided in Appendix B.

The test rig consists of following main components:

- Heater
- Levitronix pump
- Flow meter
- Temperature sensors (PT100 with 2/3 wire)
- Water supply and drain as well as interconnections with PFA-tubes
- Electrical control box including:
 - Power supply (with main switch and fuses)
 - PLC (Programmable Logic Controller with modules for digital in/outputs and analog in/outputs)
 - Transducer for flow meters
 - Solid-State-Relay for Flow Heater
 - Levitronix pump controller
 - "DIGI Connectport" - Interface converter

2. Test rig

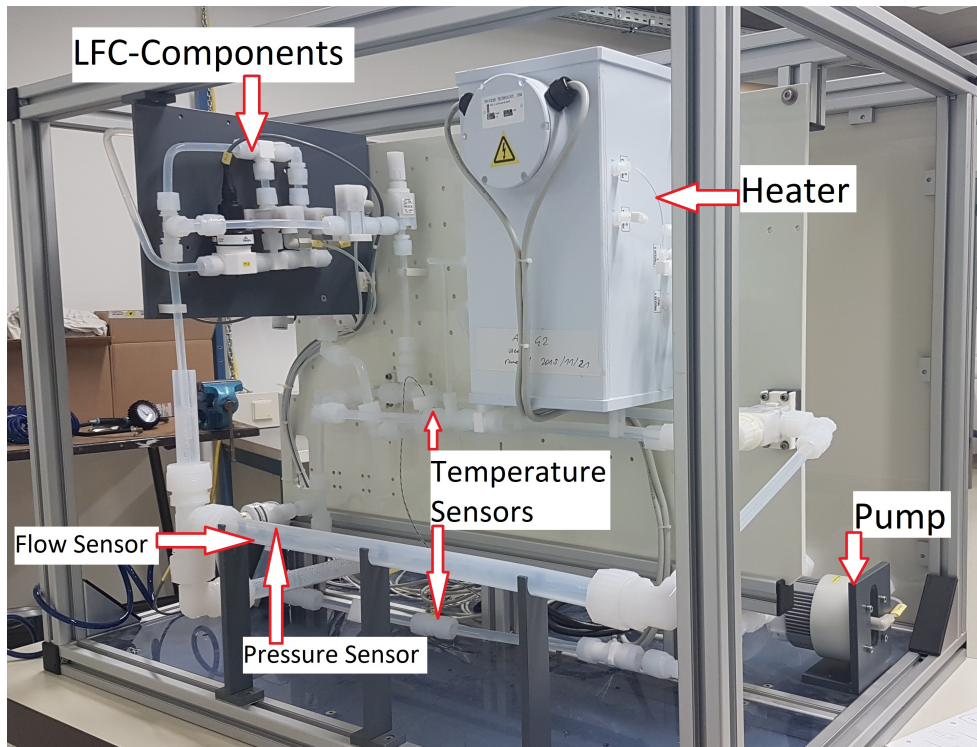


Figure 2.1.: Test rig with its components



Figure 2.2.: Test rig front side with water supply

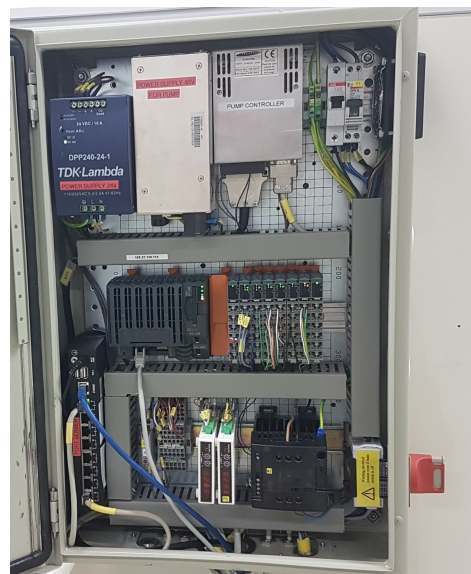


Figure 2.3.: Test rig control box

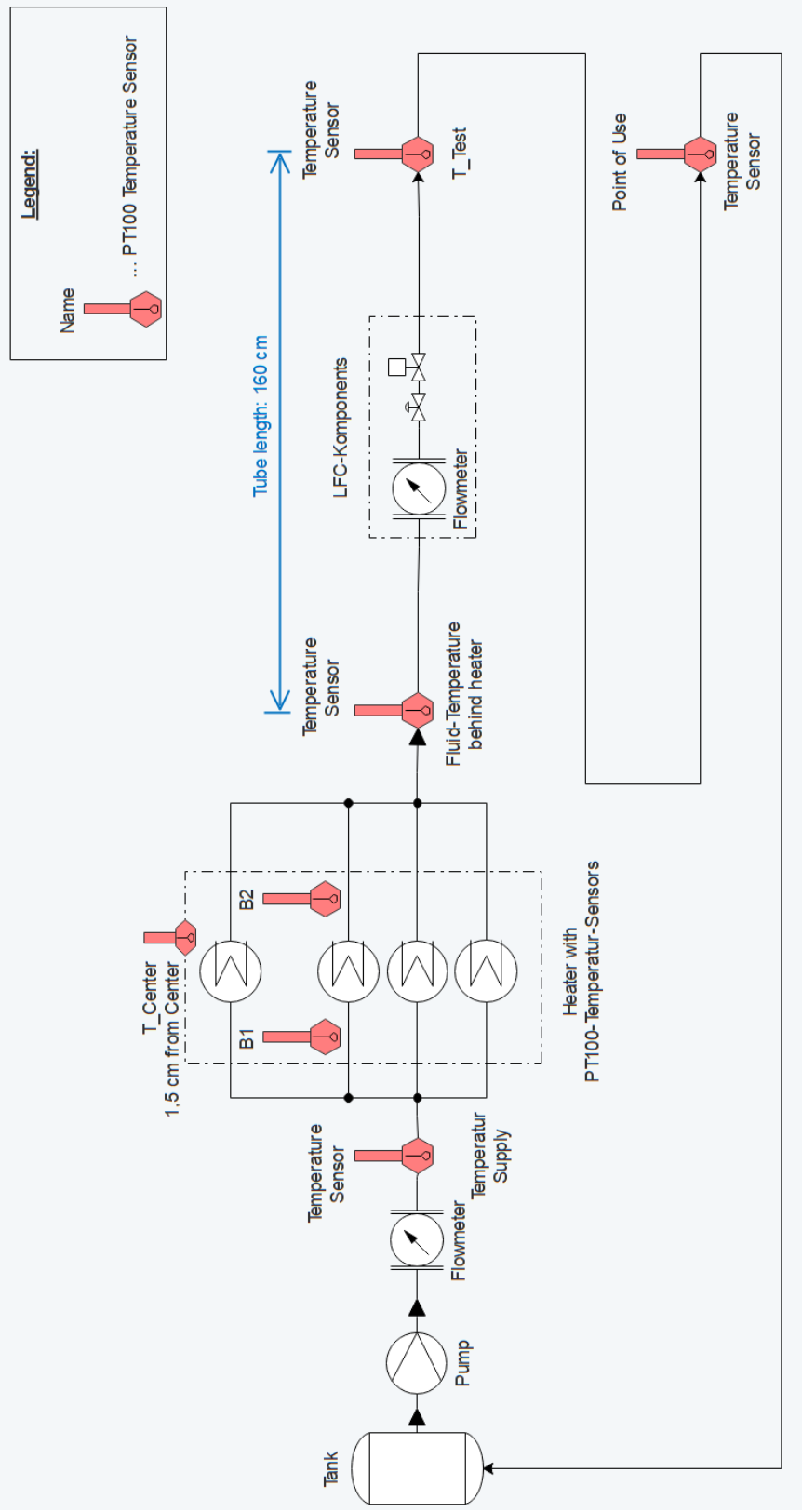


Figure 2.4.: Test rig flow plan

2. Test rig



Figure 2.5.: The flow heater

Nominal voltage	480	V
Rated current	2,9	A
Power	1400	Watt
Flow Range	0,2 - 1,2	$\frac{l}{min}$
Sum for all four streams	200 - 1200	$\frac{ml}{min}$

Table 2.1.: Heater technical Data

2.1. Description of the main components

2.1.1. Flow heater

Figure 2.5 shows the flow heater with the plastic cover. The liquid flows through four separate streams. Two PT100-Temperature sensors are installed inside the heater: One is for the control loop, and the second one is for emergency-shut-off. The heater is specially designed for semiconductor fabrication plants, which typically have a power supply with a nominal voltage of 480 V.

Table 2.1 summarizes the characteristics of the heater.

The sum of the overall volume of the four streams is approximately 63 ml; (calculated and measured). The average residence time i.e. the time the liquid requires to travel through the entire heater, is 8 seconds at a flow rate of $500 \frac{ml}{min}$.

2.1. Description of the main components

	Set	Measured
Measurement	u	P_{act}
No.	%	Watt
1	10	60
2	30	240
3	50	434
4	75	644
5	100	900

Table 2.2.: Measured values for heater characteristic curve

The characteristic curve describes the correlation of the heater input, which is the actuating variable u with the heater output, which is the thermal power. The actuating variable u has a range from 0 - 100 % which corresponds to a thermal power range from 0 - 900 W. The measured values from Table 2.2 were recorded on the test rig with European normal 400 V supply voltage. The characteristic curve is linear and the curve was fitted by a least-squares method. The measured points and the characteristic curve are shown in Figure 2.6. The zero point shift in the characteristic curve is due to the tolerance to the 4 - 20 mA signal and does not influence on the operation of the heater.

Note that the nominal voltage is 400 V, but on that day, the measured mean value of the voltage in the laboratory was 390 V, which is, according to IEC 60038, in the acceptable tolerance range.

P_{nom} ... nominal heater power

P_{act} ... actual heater power in laboratory

$$P_{nom} = \frac{U_{nom}^2}{R} \Leftrightarrow R = \frac{U_{nom}^2}{P_{nom}} = \frac{(480V)^2}{1400W} = \underline{165 \Omega} \quad (2.1)$$

$$P_{act} = \frac{U_{act}^2}{R} = \frac{(390 V)^2}{165\Omega} = \underline{900 W} \quad (2.2)$$

$$\text{Percent Power in Relation to 480 V: } \frac{P_{act}}{P_{nom}} = \frac{900}{1400} = \underline{65 \%} \quad (2.3)$$

The resistance of $R = 165 \Omega$ was checked with an ohmmeter. Due to the lower voltage in the laboratory, only 65 % of the nominal heater power is available. With an asynchronous loadable transformer for voltage increase ($\frac{400}{480}$), the nominal heating power could be used.

Heater power distribution and efficiency

The total electrical input power is converted into thermal energy within the heater.

2. Test rig

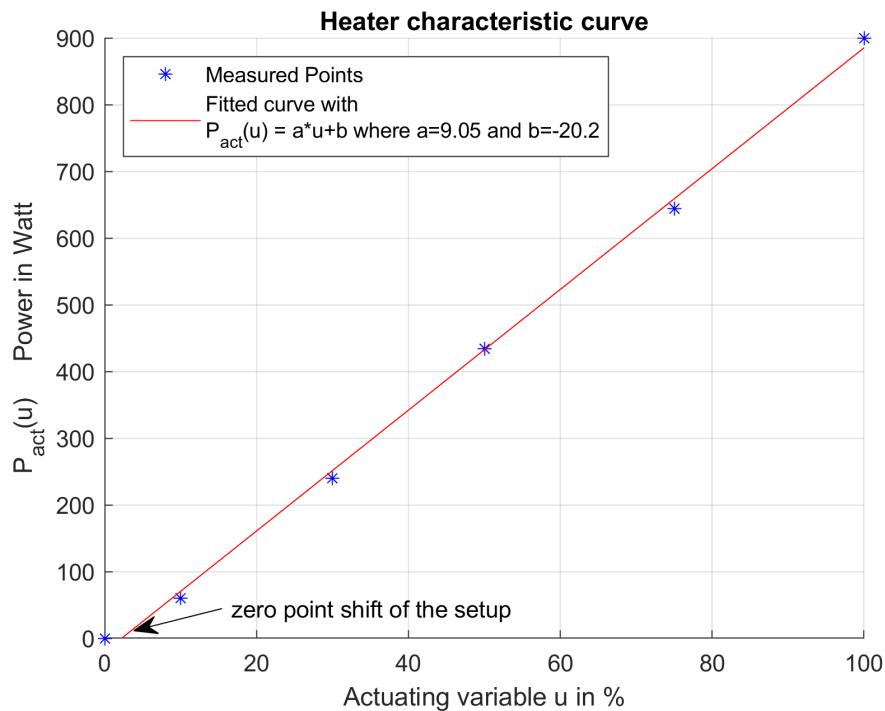


Figure 2.6.: Heater characteristic curve at 400 V supply

However, due to heat losses, only a part of it can be used to heat the liquid. The calculation of the efficiency η of the heater in steady state is shown in Table 2.1.1.

\dot{Q} ... heat flow rate
 ΔT ... temperature difference
 ϑ ... temperature
 index f ... fluid

The thermal energy is calculated according to

$$Energy = c \cdot \phi \cdot \Delta T = 4.2 \frac{J}{gK} \cdot 5 \frac{g}{s} \cdot 12.9K = \underline{271J} \quad (2.4)$$

where ϕ denotes the flow rate and c is the material's specific heat capacity. It can be seen that the calculated efficiency varies from 60 to 80%. The changes are due to the surrounding area: The first experiment has the worst efficiency, and the efficiency increases continuously with longer test duration since the experiments were performed one after the other.

2.1. Description of the main components

Measurement	Adjusted			Measured and calculated				
	ϕ		\dot{Q}	$\vartheta_{f, supply}$	$\vartheta_{f, outlet}$	ΔT	Energy	η
No.	$\frac{ml}{min}$	$\frac{ml}{s}$	Ws	$^{\circ}C$	$^{\circ}C$	K	Joule	%
1	300	5	450	23,7	36,6	12,9	271	60
2	300	5	900	23,9	54,0	30,1	632	70
3	600	10	450	23,9	31,7	7,8	328	73
4	600	10	900	23,9	40,4	16,5	639	77

Table 2.3.: Measured values for calculating the efficiency.

2.1.2. Programmable Logic Controller (PLC)

A PLCs of the B&R X20 System is used in this project. The B&R X20 is a modular system, which means that many different modules for inputs and outputs can be connected. Current PLCs, like the CPU from B&R X20, has an Ethernet port, requires an IP-Address, and can communicate via many different protocols. The development environment for the configuration and programming of the PLC is the B&R Automation Studio. Several programming languages are supported: Structured Text (ST), Function Block Diagram (FBD), Ladder Diagram (LD) according to ISO Standard IEC 61131-3, ANSI C and C++. The B&R X20 system with its I/O modules is very easy to connect, and its modules have the highest density of channels per width ¹. There are several different digital and analog input and output modules and temperature modules available. They differ in the number of input channels, sensor type connectable, and in its resolution. It can be chosen between temperature input modules for PT100/1000 sensors, NTC-sensors or thermocouples of type J, K, S, E, C, T, N, B, R. For PT100 sensors, 2-wire, 3-wire, and 4-wire configurations are available. The 4-wire-modules have a nominal resolution of 0.001 $^{\circ}C$.

2.1.3. PT100 Temperature sensors

At the test rig, there are PT100 temperature sensors installed. PT100 stands for platinum measuring resistors with a resistance of 100 Ω at 0 $^{\circ}C$. The sensors use the temperature-dependence of the material's electrical resistance. The characteristic curve is linear and has a wide temperature range. PT100 sensors are standardized in DIN EN 60571 in a range from -200 $^{\circ}C$ to 850 $^{\circ}C$. Depending on the sensors' application and housing, the price, the possible temperature range, and the response time vary.

¹<https://www.br-automation.com/en-gb/products/io-systems/x20-system/>

2. Test rig

2.2. Test rig usage

The test rig was used during the thesis for model identification and controller tests. The software environment was MATLAB/Simulink with the B&R Automation Studio Toolbox (Target for Simulink). Figure 2.7 shows the diagram for automatic code generation and also the bidirectional data exchange when Simulink is running in so-called "external mode"².

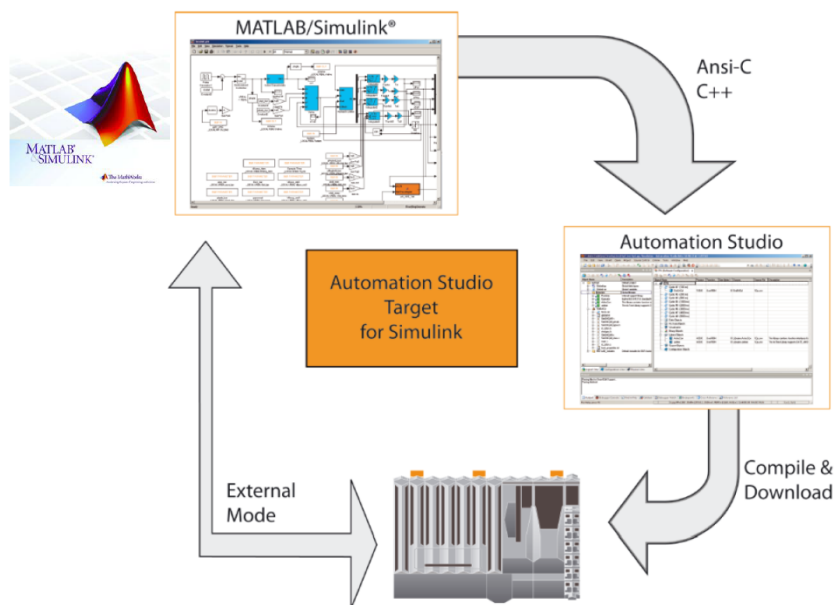


Figure 2.7.: Automation Studio Target for Simulink.

The licensed toolbox enables rapid prototyping for control-loops on PLCs and offers data post-processing with MATLAB³⁴.

The Levitronix pump with pump-controller and the flowmeters can be parametrized and adjusted via the Levitronix service software. The communication interfaces are interconnected with the PC through the "DIGI Connectport".

²<https://www.mathworks.com/content/dam/mathworks/mathworks-dot-com/solutions/automotive/files/de-expo-2014/model-based-development-in-industrial-automation-the-example-of-a-pdf>

³https://de.mathworks.com/products/connections/product_detail/br-automation-studio.html,

⁴<https://www.br-automation.com/de-at/produkte/software/modellierung-und-simulation/automation-studio-target-for-simulink/>

3. Mathematical modelling

In this section a physically motivated model of the heater will be presented. Therefore, in a first step the structure of the heater is explained. The heater basically is a aluminium cylinder with radius $r_b = 5$ cm and $h = 30$ cm with tubes wrapped around, see Figure 3.1. Outside the tubes, there is an insulation layer to reduce heat losses. In the center of the metal cylinder, there is a heating cartridge with electrical connectors. Normally there are two temperature sensors installed in the heater. The third temperature sensor in the center has been installed for measuring the temperature close to the heating cartridge.

The controlled variable is the temperature at the outside of the aluminium body.

3.1. The one-dimensional heat equation

Fourier's law, also known as the law of heat conduction, states that the heat flow rate through a material is proportional to the negative temperature gradient. For homogeneous, isotropic materials the local heat flux density \dot{q} is equal to the product of the thermal diffusivity κ and the negative local temperature gradient $-\nabla\vartheta(t, \mathbf{x})$. The Fourier's law can be written in differential form as:

$$\dot{q}(t, \mathbf{x}) = -\kappa \nabla \vartheta(t, \mathbf{x}) \quad (3.1)$$

with

\dot{q} ... is the local heat flux density

κ ... is the material's thermal diffusivity

$\nabla \vartheta$... is the temperature gradient

where

$$\kappa = \frac{\mu}{\rho c} \quad (3.2)$$

3. Mathematical modelling

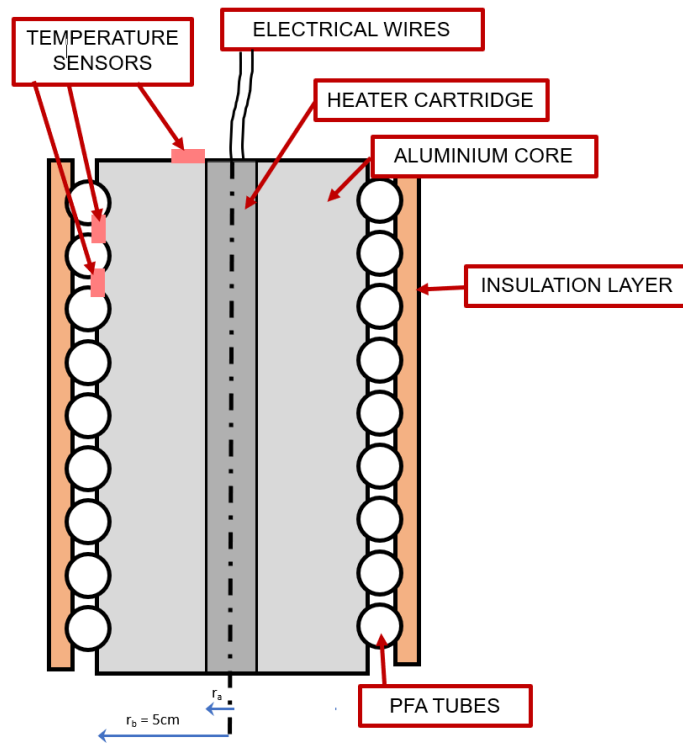


Figure 3.1.: Cross-sectional view of the heater

- μ ... thermal conductivity
- ρ ... material's specific density
- c ... material's specific heat capacity

When considering a fixed volume v without material movement there can be with the principle of conservation of energy the following relationship inferred:

$$\int_V \rho c_p(x, \vartheta) \frac{\partial \vartheta(t, x)}{\partial t} dv = - \underbrace{\int_{\partial v} \dot{q}(t, x) \cdot ndA}_{=\dot{Q}} + \underbrace{\int_V g(t, x, \vartheta) dv}_{=P}, \quad (3.3)$$

where \dot{Q} describes the heat flow into the considered volume, and P is energy brought into the system by power. An example of g would be the heat generation at an electrical resistance.

The deduction of the heat equation is by applying the Gaussian integral theorem onto Equation (3.3) and then insert Equation (3.1).

The heat equation in cylindrical coordinates for temperature ϑ at the point r ,

3.2. Model with the heating cartridge as heat source

simplified for only radially heat flow, reads as

$$\rho c \frac{\partial \vartheta(r, t)}{\partial t} = \mu \left(\frac{\partial^2 \vartheta(r, t)}{\partial r^2} + \frac{1}{r} \frac{\partial \vartheta(r, t)}{\partial r} \right) \quad (3.4)$$

which is a differential equation and describes the temperature for $r \in (0, r_b)$ and $t > 0$. For solving the equation, initial and boundary conditions are necessary.

3.2. Model with the heating cartridge as heat source

The model described in this section assumes that the heating cartridge has a radius of $r_a = 7$ mm. A validation of the model is given in Section 3.4. The model consists of the heat equation, the boundary conditions, and initial values. The Neumann boundary conditions at the contact surface $r = r_a$ is

$$-\mu \frac{\partial \vartheta(r, t)}{\partial r} \Big|_{r=r_a} = \dot{Q}_{hc} = \eta u \quad (3.5)$$

where u is the actuating variable with its feasible range 0 – 100 % of the percent power introduced into the system, set as duty cycle with the solid-state relay.

The positive constant η is a scaling factor for the relation to the introduced power. The boundary condition at radius $r = r_b$ is

$$-\mu \frac{\partial \vartheta(r, t)}{\partial r} \Big|_{r=r_b} = \dot{Q}_{cf} = \alpha(\phi)(\vartheta_f - \vartheta(r_b, t)) \quad (3.6)$$

where $\alpha(\phi)$ is the heat transfer coefficient in $\frac{W}{m^2K}$. The heat transfer coefficient depends on the volumetric flow rate ϕ and is modelled by:

$$\alpha(\phi) = \mu(k_1 + k_2\phi) \quad (3.7)$$

with k_1 and k_2 are plant specific factors. Figure 3.2 shows the top view of the heater with drawn boundary conditions.

The heat equation is spatially discretized by replacing the spatial derivatives by the central difference quotient

$$\frac{\partial \vartheta(r, t)}{\partial r} \approx \frac{\vartheta(r + \Delta r, t) - \vartheta(r - \Delta r, t)}{2\Delta r}, \quad (3.8)$$

$$\frac{\partial^2 \vartheta(r, t)}{\partial r^2} \approx \frac{\vartheta(r + \Delta r, t) - 2\vartheta(r, t) + \vartheta(r - \Delta r, t)}{(\Delta r)^2}. \quad (3.9)$$

The radius of the metal core is divided into n equidistant nodes, with distance

$$\Delta r = \frac{r_b - r_a}{n}. \quad (3.10)$$

3. Mathematical modelling

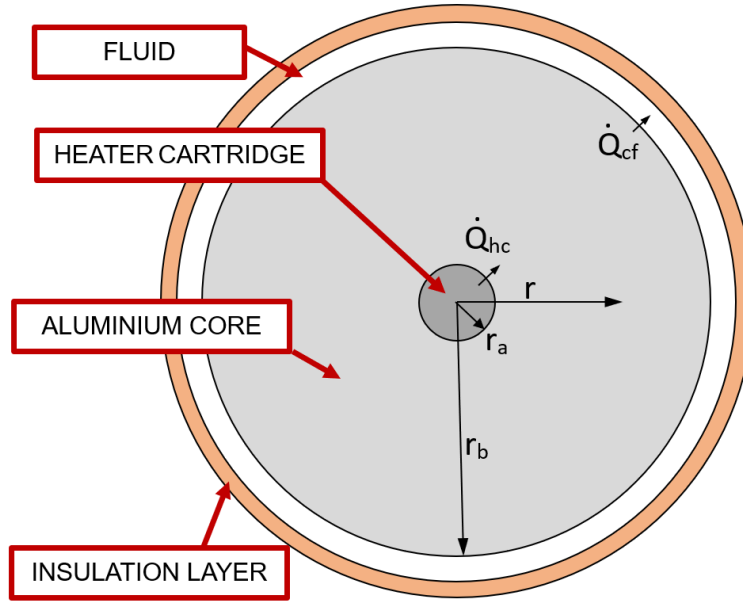


Figure 3.2.: Top view of the heater with marked boundary conditions.

This approach leads to the ordinary differential equations

$$\frac{d\vartheta_i}{dt} = \frac{\kappa}{(\Delta r)^2} [(1 - \chi_i)\vartheta_{i-1} - 2\vartheta_i + (1 + \chi_i)\vartheta_{i+1}], \quad i = 1, 2, \dots, n-1, \quad (3.11)$$

$$\text{where } \vartheta_i := \vartheta(r_i, t) \quad (3.12)$$

$$\text{and } \chi_i := \frac{1}{2\left(\frac{r_a}{\Delta r} + i\right)}. \quad (3.13)$$

When inserting the boundary conditions given in equation (3.5) and (3.6) into (3.11) the following equations are obtained:

$$\frac{d\vartheta_0}{dt} = \frac{\kappa}{(\Delta r)^2} [2\vartheta_1 - 2\vartheta_0 + 2(1 - \chi_0)\Delta r \frac{\alpha}{\mu} u], \quad (3.14)$$

$$\frac{d\vartheta_n}{dt} = \frac{\kappa}{(\Delta r)^2} [2\vartheta_{n-1} + 2(1 + \chi_n)\Delta r \frac{\alpha}{\mu} \vartheta_f - 2(1 + (1 + \chi_n)\Delta r \frac{\alpha}{\mu})\vartheta_n]. \quad (3.15)$$

Finally the equations (3.11), (3.14) and (3.15) can be written as state-space-modell in the form

$$\frac{dx}{dt} = Ax + bu + f\vartheta_f \quad (3.16)$$

$$y = c^T x \quad (3.17)$$

3. Mathematical modelling

3.2.1. Temporal discretization

The discrete-time state-space model is:

$$\mathbf{x}_{k+1} = \mathbf{A}_d \mathbf{x}_k + \mathbf{b}_d u_k + \mathbf{f}_d \vartheta_{fk}, \quad (3.22)$$

$$y_k = \mathbf{c}_d^T \mathbf{x}_k, \quad (3.23)$$

$$\text{with } \mathbf{x}_k = \mathbf{x}(t = kT_d). \quad (3.24)$$

For continuous to discrete conversion, the Zero-Order-Hold method provides an exact discretization in the time domain:

$$\begin{bmatrix} \mathbf{A}_d & \mathbf{b}_d \\ 0 & 1 \end{bmatrix} = e^{\begin{bmatrix} \mathbf{A} & \mathbf{b} \\ 0 & 0 \end{bmatrix} T_d}, \quad \mathbf{c}_d^T = \mathbf{c}^T \quad (3.25)$$

where T_d is the sampling time. An other approximation of the continuous time system is obtained by Taylor series expansion of Equation (3.25) and truncating after the linear term, which gives

$$\mathbf{A}_d := \mathbf{E} + T_d \mathbf{A} \quad (3.26)$$

$$\mathbf{b}_d := T_d \mathbf{b} \quad (3.27)$$

$$\mathbf{f}_d := T_d \mathbf{f} \quad (3.28)$$

$$\mathbf{c}_d^T := \mathbf{c}^T \quad (3.29)$$

where \mathbf{E} denotes the identity matrix. The expression $\mathbf{E} + T_d \mathbf{A}$ must be a Hurwitz matrix. If it is not, varying T_d is possible. This method simplifies parameter identification: Parameters identified for this discrete-time model can be easily converted for the continuous time model.

3.2.2. Parameter identification

Parameters from the model which are not known are determined with the following parameter identification. The parameters and their results are listed in Table 3.2. The parameters are identified by comparison measured data from the real plant with the values from a simulation of the mathematical model, where the factors are adjusted. Equation (3.30) shows the cost function which is optimized for parameter identification with the method of the least square error:

$$\min \sum_{i=1}^N e_i^2, \quad \text{where } N \text{ is the total number of sampled points.} \quad (3.30)$$

The scalar e_i denotes the difference from the computer model to measured data at time $t = i \cdot T_d$.

3.2. Model with the heating cartridge as heat source

	Symbol	Start value	Optimization result	Unit
Power factor	η	1364	950.8	$\frac{W}{m^2}$
Constant k1	k1	2	0.01	1
Constant k2	k1	18	63.8	1
Cylinders conductivity	μ	30	16.1	$\frac{W}{mK}$
Heat capacity	c	900	1264.9	$\frac{J}{kgK}$
Density	ρ	2700	2115.6	$\frac{kg}{m^3}$

Table 3.2.: Start values and optimized values for modell ra and rb

The sampling rate has to be high enough, that the system is stable. The recorded data has a sampling rate of one second, which is instable with the discrete-time state model from Equation (3.26). A 20-times up-sampling was used to get $T_d = 0.05$ seconds. The approximation for the time-discrete system is together with the least square error used for parameter identification:

The start values are calculated:

$$\eta = \frac{P_{max}}{100 \cdot (2\pi r_a \cdot h)} = \frac{900W}{100\% \cdot 2 \cdot \pi \cdot 0.007m \cdot 0.3m} = \underline{\underline{1364 \frac{W}{m^2}}} \quad (3.31)$$

Table 3.2 shows the start values and the parameters obtained from the optimization.

The optimization (identification of parameters) was done with experiments measured and sampled on the test rig. The data were concatenated to a nine-hours-sequence, which is shown in Figure 3.3. The MATLAB-optimization algorithm "fminsearch" was used.

Figure 3.4 shows an experiment with a duration of 60 Minutes data recording at constant flow $\phi = 600 \frac{ml}{min}$ and constant input temperature. When the heater is switched on, the fluid output temperature is a few degrees lower than the controlled variable.

Validation and comparison of measured and simulated data are in Section 3.4.

3. Mathematical modelling

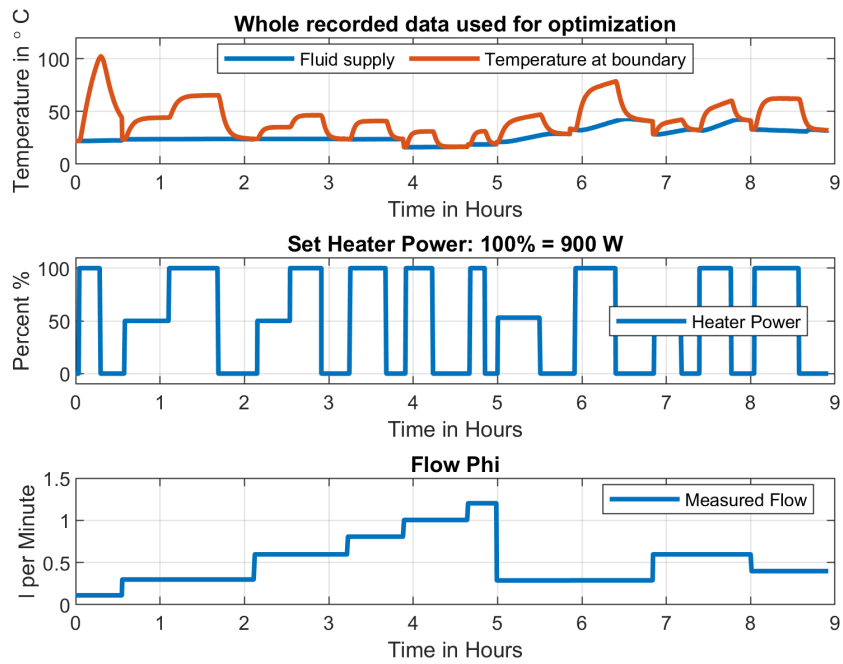


Figure 3.3.: Measured data for optimization

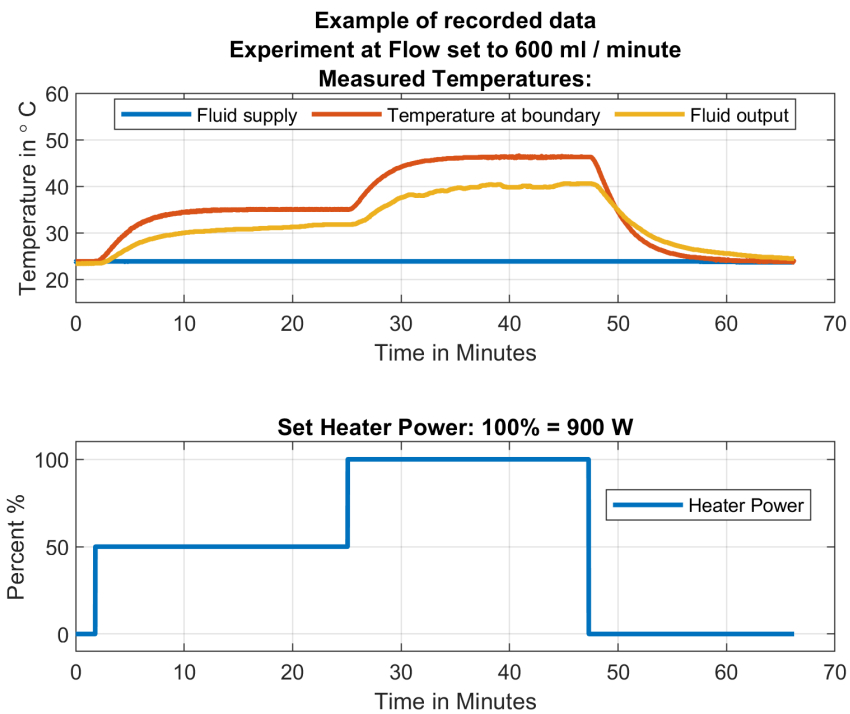


Figure 3.4.: Example of recorded data

3.3. Model with indefinite small heat source

Simplifying the mathematical model is done by considering the limit $r_a \rightarrow 0$. That means that the heating source is modeled as an indefinite small heat source. It is assumed that the whole metal cylinder (including the heating cartridge) has the same heat-conduction-coefficient.

The heat equation in cylindrical coordinates is

$$\frac{\partial \vartheta(r, t)}{\partial t} = \kappa \left(\frac{\partial^2 \vartheta(r, t)}{\partial r^2} + \frac{1}{r} \frac{\partial \vartheta(r, t)}{\partial r} \right) + \frac{\dot{Q}(r, t)}{mc} \quad (3.32)$$

with $r \in (0, r_b)$. The boundary conditions at center and the contact surface are of Neumann type and given by

$$\frac{\partial \vartheta(r, t)}{\partial r} \Big|_{r=0} = 0 \text{ and } \frac{\partial \vartheta(r, t)}{\partial r} \Big|_{r=r_b} = 0. \quad (3.33)$$

Discretization in space is done by replacing the spatial derivatives by the central difference quotient. The radius of the metal core is divided into n equidistant distances, i.e.,

$$\Delta r = \frac{R}{n}. \quad (3.34)$$

The obtained set of ordinary differential equations then read as

$$\frac{d\vartheta_{h,i}}{dt} = \frac{\kappa}{(\Delta r)^2} \left[\left(1 + \frac{1}{2\chi_i}\right) \vartheta_{h,i-1} - 2\vartheta_{h,i} + \left(1 - \frac{1}{2\chi_i}\right) \vartheta_{h,i+1} \right] + \frac{\dot{Q}_i(r, t)}{mc}, \quad (3.35)$$

$$i = 1, 2, \dots, n, \quad (3.36)$$

$$\vartheta_{h,i} := \vartheta_h(r_i, t), \quad (3.37)$$

$$\text{with } \chi_i := \frac{2i-1}{2}. \quad (3.38)$$

The heater is power is in the innermost element as

$$\dot{Q}_1 = \eta n. \quad (3.39)$$

The heat transfer from the metal body to the fluid is described by

$$\dot{Q}_n = \alpha(\phi) A (\vartheta_f - \vartheta_{h,n}) \quad (3.40)$$

3. Mathematical modelling

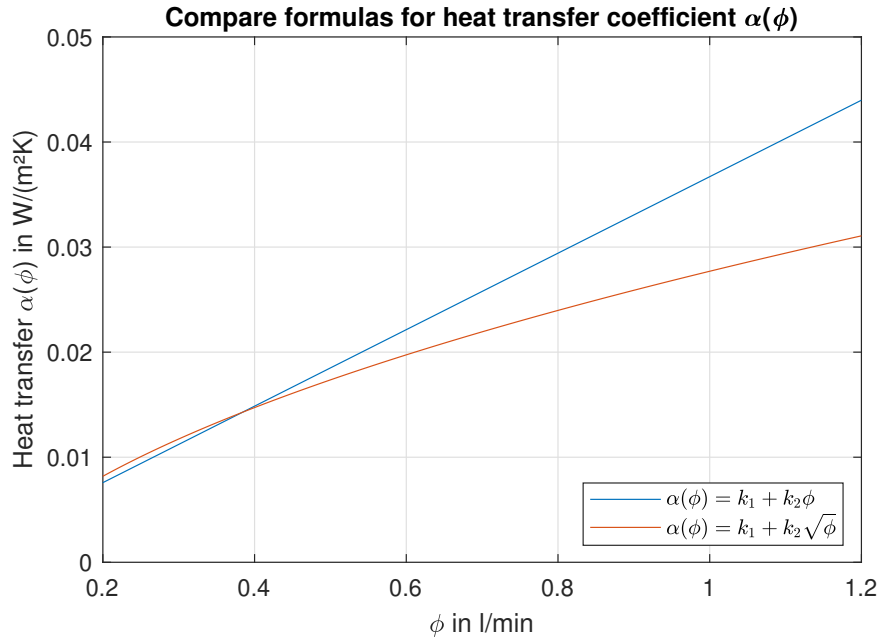


Figure 3.5.: Comparison of two formulas for the heat transfer coefficient

see [5]. Two equations are compared for the heat transfer coefficient, normally

$$\alpha(\phi) = k_1 + k_2\sqrt{\phi} \quad \text{or} \quad (3.41)$$

$$\alpha(\phi) = k_1 + k_2\phi \quad (3.42)$$

A comparison between Equations (3.41) and (3.42) is shown in Figure 3.5. Equation (3.41) produces the smaller value at the cost function, see Table 3.3.

The state-space model has the form:

$$\frac{dx}{dt} = Ax + bu + f\vartheta_f \quad (3.43)$$

$$y = c^T x \quad (3.44)$$

where $x \in \mathbb{R}^{(n)}$. The tridiagonal Matrix A is

$$A = \underbrace{\frac{\kappa}{(\Delta r)^2}}_{=: \lambda_3} \begin{bmatrix} -1 - \frac{1}{2\chi_1} & 1 + \frac{1}{2\chi_1} & & & \\ 1 - \frac{1}{2\chi_1} & -2 & \ddots & & 0 \\ & \ddots & \ddots & \ddots & \\ & & 0 & \ddots & -2 \\ & & & 1 - \frac{1}{2\chi_n} & -1 + \frac{1}{2\chi_n} - \frac{1 + \frac{1}{2\chi_{n-1}}}{mc} \frac{\alpha(\phi)A(\Delta r)^2}{\kappa} \end{bmatrix} \quad (3.45)$$

3.4. Validation and comparison of models

	Symbol	Start value	Optimization result using Equation (3.41)	Optimization result using Equation (3.42)
Factor	λ_1	0.0008	-0.0076	0.0003
Factor	λ_2	0.001	0.0353	0.0364
Factor	λ_3	0.0352	0.0297	0.0291
Heater scaling factor	b_1	0.0371	0.0314	0.0318
Cost function	-	-	89212.1	89362.6

Table 3.3.: Start values and optimized values for $r_a \rightarrow 0$

and the vectors

$$\mathbf{f} = \begin{bmatrix} 0 & 0 & \dots & 0 & \underbrace{\frac{\alpha(\phi)A}{mc}}_{=:\lambda_1+\lambda_2\sqrt{\phi}} \end{bmatrix}^T \quad (3.46)$$

$$\mathbf{b} = \begin{bmatrix} \underbrace{\frac{\eta}{mc}}_{=:b_1} & 0 & \dots & 0 & 0 \end{bmatrix}^T \quad (3.47)$$

$$\mathbf{c}^T = [0 \ 0 \ \dots \ 0 \ 1]^T \quad (3.48)$$

The optimization was done with $n = 4$. It requires low computing power, and it is sufficiently accurate. The results are shown in Table 3.3.

In Equation (3.6) and (3.40) the fluid temperature ϑ_f appears. However, it is not clear whatever this is the fluid inlet or outlet temperature, as the model neglects the temperature distribution in z -direction. The cost function was lower when taking the fluid inlet temperature.

3.4. Validation and comparison of models

The models were validated by comparing obtained results gained by experimental data not used for identification. The different test conditions are shown in Figure 3.6. Figure 3.7 shows that the error remains in a ± 2 degree range.

The model with indefinite small heat source has the advantage that the time discretization with truncating after the first Taylor coefficient works without up-sampling when having $T_d = 1s$. The other model requires up-sampling.

3. Mathematical modelling

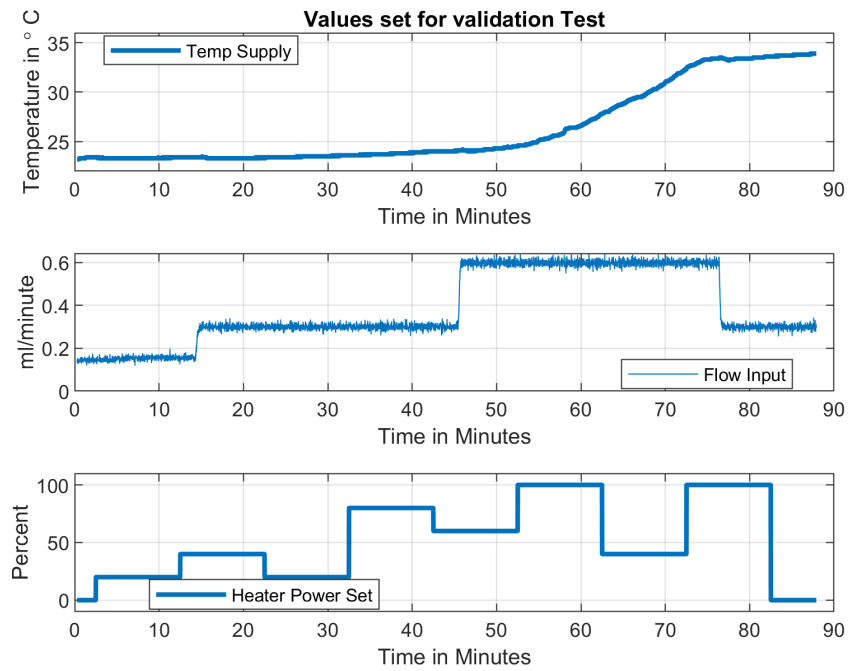


Figure 3.6.: Different input conditions for validating the Models

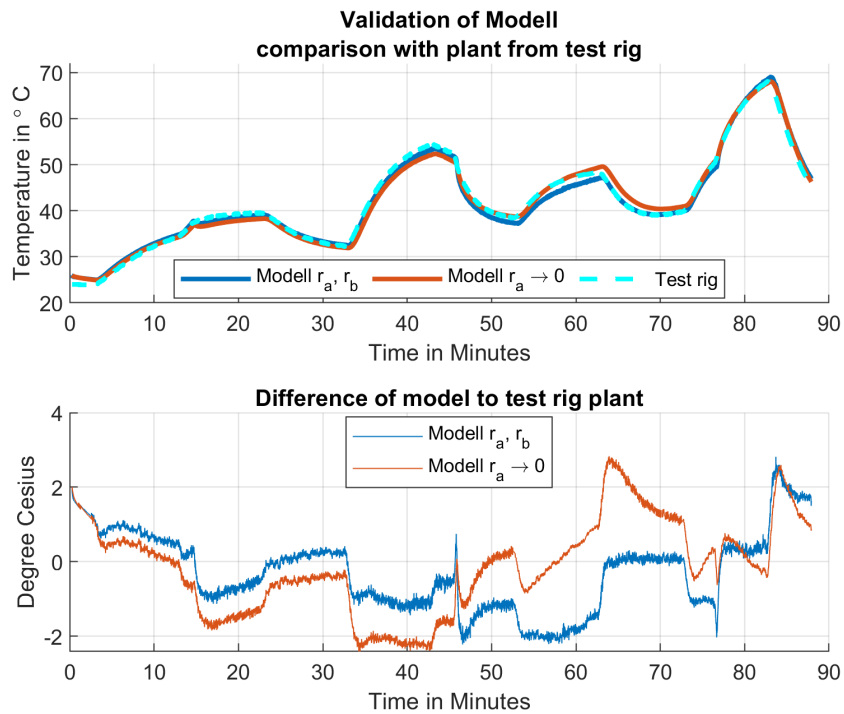


Figure 3.7.: Validation and comparison of the Models

3.4. Validation and comparison of models

Concluding remarks:

The advantage of the physically motivated model is that it also can be adapted to other heater types.

The control-algorithms described in the next two sections use the model with $r_a \rightarrow 0$ from Section 3.3 with Equation (3.41).

Since the accuracy of the model is sufficiently accurate for the purpose of controller design, the simplification (neglecting temperature distribution in z-direction) is reasonable.

4. Disturbance observer-based linear state feedback controller

Parts of this chapter are derived from "Model-based Temperature Control of a Continuous Flow Heater for Efficient Processing of Silicon Wafers" [5] which is an article presented at the 4th IEEE CCTA.

The design goal is to find a control law such that the cylinder temperature at $r = r_b$ tracks a constant reference temperature. In this chapter a disturbance observer-based state feedback controller is designed and test results are presented. Since the state vector x of the system model from Equation (3.43) cannot be measured, a state observer is required. The observer is described in the next section.

4.1. Luenberger observer

Observers are used in control engineering for estimating non-measurable system states. The observer uses as basis the mathematical plant model proposed in Section 3.3 with system order $n = 4$. A requirement for the design of an observer is the observability of the system. The observability is checked with the Kalman criteria. The observability matrix \mathcal{O} calculates as

$$\mathcal{O} = \begin{bmatrix} c^T \\ c^T A \\ \vdots \\ c^T A^{n-1} \end{bmatrix} = \begin{bmatrix} 0 & 0 & 0 & 1.0000 \\ 0 & 0 & 0.0255 & -0.0428 \\ 0 & 0.0006 & -0.0026 & 0.0027 \\ 0.000 & -0.0001 & 0.0002 & -0.0002 \end{bmatrix}. \quad (4.1)$$

The system is observable, because the observability matrix \mathcal{O} is has rank $n = 4$.

The Luenberger observer for system (3.43) is given by the following equation:

$$\dot{\hat{x}} = A\hat{x} + bu + l(y - \hat{y}) \quad (4.2a)$$

$$\hat{y} = c^T \hat{x} \quad (4.2b)$$

4. Disturbance observer-based linear state feedback controller

where $\hat{x} \in \mathbb{R}^n$ is the estimated state vector, \hat{y} us the estimated output and $l \in \mathbb{R}^n$ is the observer gain. The estimation error e is defined as the difference between the state vector x and the estimated state vector \hat{x} i.e.,

$$e := x - \hat{x}. \quad (4.3)$$

In Equation (3.43) the input ϑ_f is assumed as constant disturbance, i.e., $\frac{d\vartheta_f}{dt} \approx 0$. Please note that the temperature ϑ_f , which denotes the fluid temperature, is not measurable and the observer is used to estimate this quantity too.

For developing the observer, the derivative w.r.t time at the estimation error (4.3) is computed:

$$e = x - \hat{x} \quad \Leftrightarrow \quad \dot{e} = \dot{x} - \dot{\hat{x}} \quad (4.4)$$

Inserting the Equation (4.2a) and (4.2b) into Equation (4.4) yields

$$\dot{e} = Ax + bu + f\vartheta_f - [A\hat{x} + bu + l(y - c^T\hat{x})] \quad (4.5a)$$

$$\dot{e} = A(\underbrace{x - \hat{x}}_e) + f\vartheta_f - l(c^T x - c^T \hat{x}) \quad (4.5b)$$

$$\dot{e} = Ae - lc^T e + f\vartheta_f \quad (4.5c)$$

$$\dot{e} = (A - lc^T)e + f\vartheta_f \quad (4.5d)$$

The disturbance $\vartheta_f \neq 0$ prevents the estimation error from converging to zero. The steady-state estimation error is

$$e_\infty := \lim_{t \rightarrow \infty} e(t). \quad (4.6a)$$

For constant ϑ_f the equilibrium computes as

$$\dot{e}_\infty \stackrel{!}{=} 0 = (A - lc^T)e_\infty + f\vartheta_f, \quad (4.7a)$$

$$-(A - lc^T)e_\infty = f\vartheta_f, \quad (4.7b)$$

$$e_\infty = -(A - lc^T)^{-1} f\vartheta_f. \quad (4.7c)$$

The error between the measured and estimated output yields

$$c^T e_\infty = \Delta y_\infty = -(A - lc^T)^{-1} f\vartheta_f. \quad (4.8)$$

From (4.5c) the disturbance is estimated as

$$\vartheta_f = \Delta y_\infty \frac{-1}{c^T (A - lc^T)^{-1} f}. \quad (4.9)$$

4.2. Design of the state feedback controller

Substituting Equation (4.9) into Equation (4.7c) yields

$$e_{\infty} = \Delta y_{\infty} \frac{(A - lc^T)^{-1} f}{c^T (A - lc^T)^{-1} f} \quad (4.10)$$

using Equation (4.10) a corrected state vector \bar{x} can be computed by

$$\bar{x} := \hat{x} + e_{\infty} = \hat{x} + \Delta y_{\infty} \frac{(A - lc^T)^{-1} f}{c^T (A - lc^T)^{-1} f}. \quad (4.11)$$

In steady state the expression $\lim_{t \rightarrow \infty} x - \bar{x} = \mathbf{0}$ holds. The observer gain was calculated by the means of the linear-quadratic regulator (LQR) approach with weighting Matrix $Q = E$ and $r = 1$ as

$$l^T = [0.1692 \quad 0.2051 \quad 0.3000 \quad 0.9657]. \quad (4.12)$$

For the computation of the dynamic matrix A , the liquid flow rate was set to nominal flow $500 \frac{ml}{min}$.

The eigenvalues of $(A^T - cl^T)$ are $[-1.0015 \quad -0.0165 \quad -0.1062 \quad -0.0625]$.

4.2. Design of the state feedback controller

The design of the state feedback controller is a method of control-loop-design in the time domain. The goal is that the output variable y of the existing plant shown in Equation (3.43) tracks a constant reference temperature r . The control-loop, consisting out of the controller, the observer, and the plant, should be asymptotically stable. The system's controllability is checked with the Kalman criteria. The controllability Matrix \mathcal{C} calculates as

$$\mathcal{C} = [b \quad Ab \quad \dots \quad A^{n-1}b] = \begin{bmatrix} 0.0314 & -0.0019 & 0.148 \cdot 10^{-3} & -0.0132 \cdot 10^{-3} \\ 0 & 0.622 \cdot 10^{-3} & -0.074 \cdot 10^{-3} & 0.008 \cdot 10^{-3} \\ 0 & 0 & 0.015 \cdot 10^{-3} & -0.003 \cdot 10^{-3} \\ 0 & 0 & 0 & 0.0004 \cdot 10^{-3} \end{bmatrix}. \quad (4.13)$$

The system is controllable, because the controllability matrix \mathcal{C} is a regular matrix.

The control law is designed as

$$u = -k^T \bar{x} - \varphi + Vr, \quad (4.14)$$

4. Disturbance observer-based linear state feedback controller

where $k \in \mathbb{R}^n$ and $V \in \mathbb{R}$ are constant gains and $\varphi \in \mathbb{R}$ is a scalar signal for compensating the unknown disturbance. Inserting the control law into the Equation of the plant (3.43) leads to the closed control loop:

$$\dot{x} = \frac{dx}{dt} = Ax - bk^T \bar{x} - b\varphi + bVr + f\vartheta_f \quad (4.15a)$$

$$y = c^T x \quad (4.15b)$$

For $t \rightarrow \infty$ the output y should track the reference value, i.e.,

$$\lim_{t \rightarrow \infty} y(t) = r. \quad (4.16)$$

This also implies, that the state vector x for $t \rightarrow \infty$ converges to a constant value x_∞ stated as

$$\dot{x}_\infty = \mathbf{0} = (A - bk^T)x_\infty - b\varphi + bVr + f\vartheta_f. \quad (4.17)$$

The state vector in an equilibrium is calculated as

$$x_\infty = (A - bk^T)^{-1}(b\varphi - f\vartheta_f) - (A - bk^T)^{-1}bVr, \quad (4.18)$$

and inserting leads to

$$y_\infty = c^T x_\infty = c^T (A - bk^T)^{-1}(b\varphi - f\vartheta_f) - \underbrace{c^T (A - bk^T)^{-1}bVr}_{\stackrel{!}{=}1}. \quad (4.19)$$

Where then V is calculated to

$$V = \frac{-1}{c^T (A - bk^T)^{-1}b} \quad (4.20)$$

and

$$\varphi = -\frac{c^T (A - bk^T)^{-1}f}{c^T (A - bk^T)^{-1}bc^T (A - bk^T)^{-1}f} \Delta y_\infty \quad (4.21)$$

Inserting Equation (4.11) and Equation (4.21) into Equation (4.14), gives the control law

$$u = -k^T \hat{x} + M \Delta y_\infty + Vr \quad (4.22)$$

with

$$M = \frac{c^T (A - bk^T)^{-1}(E - bk^T (A - lc^T)^{-1})f}{c^T (A - bk^T)^{-1}bc^T (A - lc^T)^{-1}f}. \quad (4.23)$$

Reference [5] shows that M can simplified to

$$M = \frac{1 - k^T (A - lc^T)^{-1}b}{c^T (A - lc^T)^{-1}b}, \quad (4.24)$$

4.2. Design of the state feedback controller

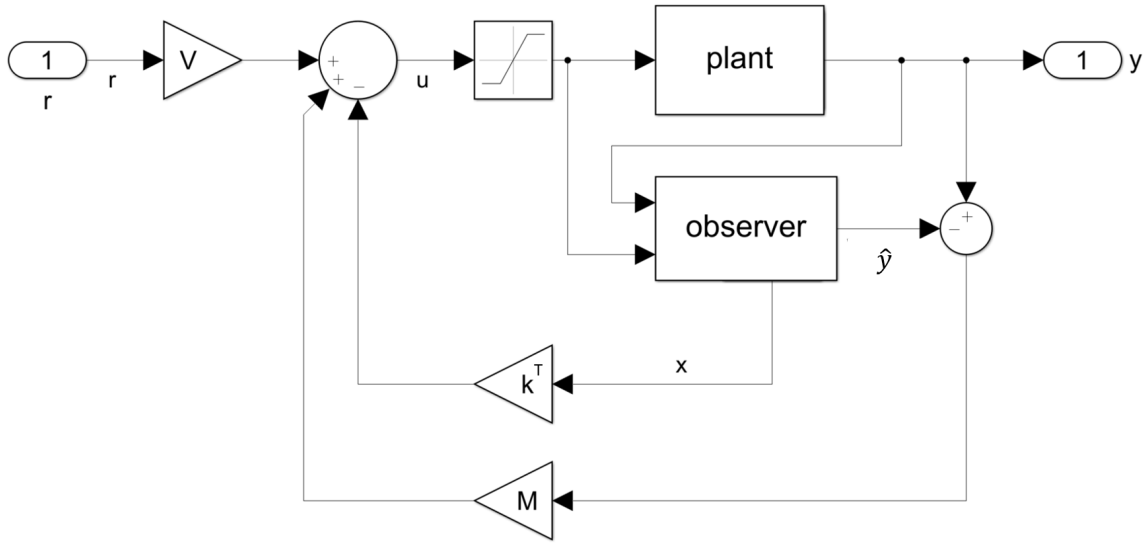


Figure 4.1.: Block diagram of the control-loop status controller

using Laplace-transformation and the so-called Sheron-Morrison formula. Since Δy_∞ is not available during execution at the real world system, it is approximated by Δy which is $\Delta y = y - c^T \cdot x$. The final control law is:

$$u = -k^T \hat{x} + M\Delta y + Vr \quad (4.25)$$

Figure 4.1 shows a block diagramm of the feedback loop.

To ensure asymptotic stability, the real part of the eigenvalues of $(A - bk^T)$ has to be negative i.e., $\Re\{\lambda_i\} < 0$.

The calculation of the controller gain was done in two steps. First a controller gain k_1^T was calculated by the means of the LQR approach with weighting Matrix $Q = E$ and $r = 0.3$. The eigenvalues s_1 were calculated from the Matrix $(A - bk_1^T)$ and afterwards multiplied with factor, so that the new eigenvalues are

$$s = s_1 \cdot 0.8 \text{ results to } s = [-0.0913 \quad -0.0663 \quad -0.0334 \quad -0.0086]^T. \quad (4.26)$$

This step is done for getting a smaller feedback gain M . The final controller gain k^T then was calculated with Ackermann's formula to

$$k^T = [-0.6817 \quad 1.9784 \quad -1.3487 \quad 0.9081]. \quad (4.27)$$

For the computation of the dynamic matrix A , the liquid flow rate was set to nominal flow $500 \frac{ml}{min}$. The gain M is calculated to -278.9870 and $V = 4.6226$.

4. Disturbance observer-based linear state feedback controller

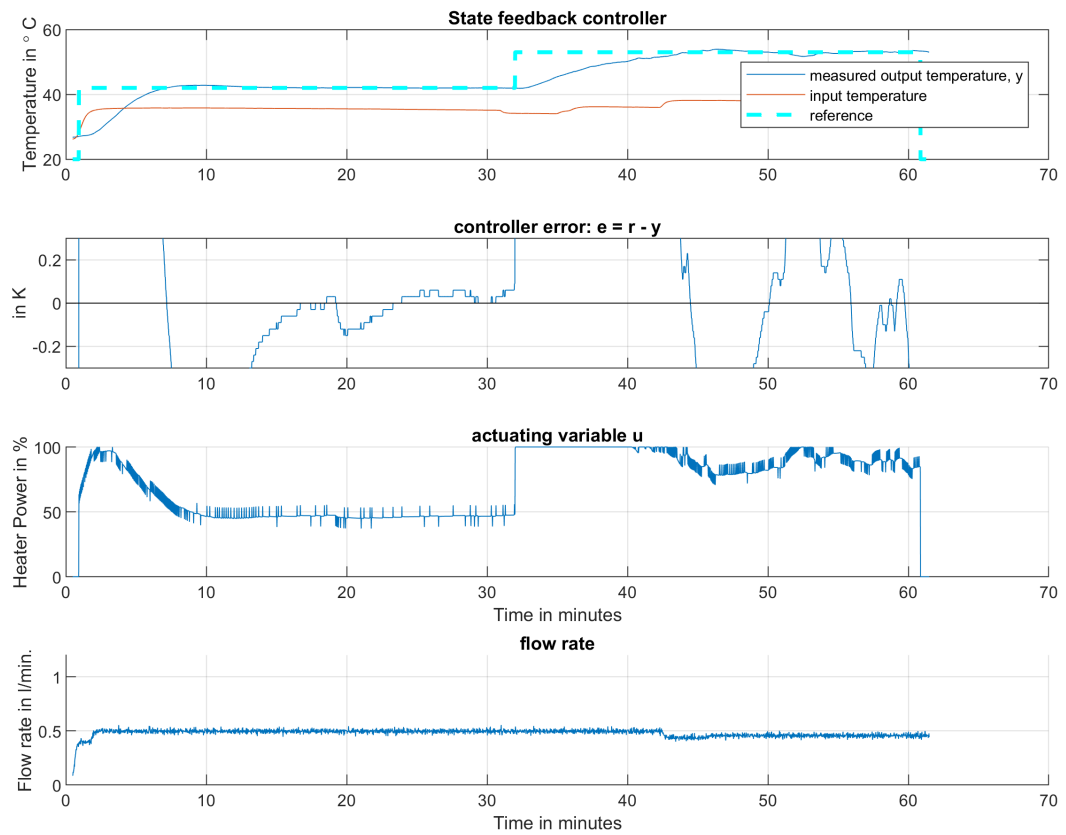


Figure 4.2.: Test results using the proposed controller obtained from the test rig.

4.3. Experimental validation

Figure 4.2 shows plots from one experiment from the proposed controller on the test rig. The controller settles in approximately 15 minutes and has an error in steady-state of $\pm 0.2^\circ\text{C}$. At changing input conditions (minute 40 to 60 in experiment) the controller also yields a constant output temperature.

During tests, the following effect was noticed: Pulse-shaped changes on the actuating variable. It was found out, that these changes came from the quantization interval of the temperature sensors, amplified with factor M . Figure 4.3 shows the behaviour with quantisation interval 0.1°C and $M = -117$ in comparison with quantisation interval 0.03°C and $M = -280$ of the controller's actuating variable. For all experiments the gain M was lower than 300, so that the effect is not too significant. If the peaks are cut off by saturation, the controller is no longer accurate. As a remedy a low pass filter with gain 1 can be built into the path. The

4.3. Experimental validation

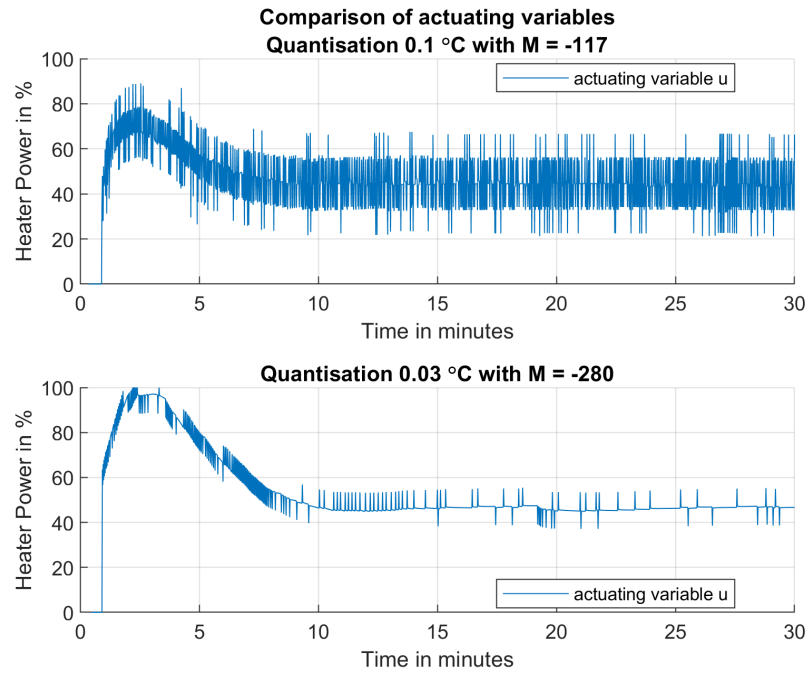


Figure 4.3.: State feedback controller - comparison of quantisation steps

time constant should be chosen such that the peaks are sufficiently smoothed.

5. Model predictive control

Model predictive control (MPC) is an advanced process control method that allows to consider constraints in the control input, the output and the state variables. MPC controllers are wide used in industry [7],[9].

Advantages of MPC:

- very good for satisfying constraints to u_k , Δu_k , x_k and y_k
- easy to scale for MIMO-systems
- no Wind-up-effect from Integrators

Disadvantages of MPC:

- high calculation complexity
- optimization is a challenge for non-linear plants

A discrete-time model of the plant is used to predict/forecast the evolution of the state variables and the output for several sampling steps. The plant is represented in the form

$$\mathbf{x}_{k+1} = \mathbf{A}_d \mathbf{x}_k + \mathbf{b}_d u_k + \mathbf{f}_d \vartheta_{fk}, \quad (5.1)$$

$$y_k = \mathbf{c}_d^T \mathbf{x}_k. \quad (5.2)$$

It is a discrete-time linear time-invariant system with sampling time T_d and

$$\mathbf{x}_k \in \mathbb{R}^n, \quad (n \text{ states})$$

$$\mathbf{u}_k \in \mathbb{R}^m, \quad (m \text{ inputs})$$

$$\mathbf{y}_k \in \mathbb{R}^p, \quad (p \text{ outputs})$$

$$\vartheta_{fk} \in \mathbb{R}^1, \quad (\text{one disturbance variable})$$

The system with the model from Section 3.3 is of order $n = 4$ (state variables) and has one actuating variable, i.e., $m = 1$, and one output variable, i.e., $p = 1$, and one disturbance variable. The matrices \mathbf{A}_d , \mathbf{b}_d , \mathbf{f}_d and \mathbf{c}_d are given in (3.26).

The reference is denoted by r_k .

The goal is to find an actuating sequence $\hat{u}_k, \hat{u}_{k+1}, \dots, \hat{u}_{k+N_c-1}$ for the control-horizon N_c , such that a cost function is minimized for the prediction horizon N_p . The cost function is calculated with the predicted plant input-, output- and state variables. The actuating variable is given in an incremental form, i.e., $u_k = u_{k-1} + \Delta u_k$ and

5. Model predictive control

the predicted actuating variable is $\hat{u}_k = u_{k-1} + \Delta\hat{u}_k$. They are collected in the vector

$$\Delta\bar{\mathbf{u}}_k = \begin{bmatrix} \Delta\hat{u}_k \\ \Delta\hat{u}_{k+1} \\ \vdots \\ \Delta\hat{u}_{k+N_c-1} \end{bmatrix} \quad \text{Dimension } (m \cdot N_c, 1) \quad (5.3)$$

The predicted state vector is iteratively defined as:

$$\hat{\mathbf{x}}_{k+1} = \mathbf{A}_d \mathbf{x}_k + \mathbf{b}_d u_{k-1} + \mathbf{b}_d \Delta u_k + \mathbf{f}_d \vartheta_{fk}, \quad (5.4a)$$

$$\hat{\mathbf{x}}_{k+2} = \mathbf{A}_d \hat{\mathbf{x}}_{k+1} + \mathbf{b}_d u_k + \mathbf{b}_d \Delta u_{k+1} + \mathbf{f}_d \vartheta_{fk}, \quad (5.4b)$$

$$\vdots \quad (5.4c)$$

$$\hat{\mathbf{x}}_{k+N_p} = \dots \quad (5.4d)$$

and are collected in the vector

$$\bar{\mathbf{x}}_{k+1} = \begin{bmatrix} \hat{\mathbf{x}}_{k+1} \\ \hat{\mathbf{x}}_{k+2} \\ \vdots \\ \hat{\mathbf{x}}_{k+N_p} \end{bmatrix} \quad \text{Dimension } (n \cdot N_p, 1) \quad (5.5)$$

The predicted outputs are defined as $\hat{y}_{k+1} = \mathbf{c}_d^T \hat{\mathbf{x}}_{k+1}$, $\hat{y}_{k+2} = \mathbf{c}_d^T \hat{\mathbf{x}}_{k+2}, \dots, \hat{y}_{k+N_p} = \mathbf{c}_d^T \hat{\mathbf{x}}_{k+N_p}$ and are collected in the vector

$$\bar{\mathbf{y}}_{k+1} = \begin{bmatrix} \hat{y}_{k+1} \\ \hat{y}_{k+2} \\ \vdots \\ \hat{y}_{k+N_p} \end{bmatrix} \quad \text{Dimension } (p \cdot N_p, 1) \quad (5.6)$$

The fluid temperature ϑ_f modelled as disturbance is collected in

$$\bar{\boldsymbol{\vartheta}}_{fk} = \begin{bmatrix} \vartheta_{fk} \\ \vdots \\ \vartheta_{fk} \end{bmatrix} \quad \text{Dimension } (p \cdot N_p, 1) \quad (5.7)$$

The future reference signal for every sampling point is collected in

$$\bar{\mathbf{r}}_{k+1} = \begin{bmatrix} \vartheta_{r_k} \\ \vdots \\ \vartheta_{r_k} \end{bmatrix} \quad \text{Dimension } (p \cdot N_p, 1) \quad (5.8)$$

The predicted output then computes as:

$$\bar{\mathbf{y}}_{k+1} = \underbrace{\mathbf{F}\mathbf{x}_k + \mathbf{G}u_{k-1} + \mathbf{H}_d\bar{\boldsymbol{\vartheta}}_{fk}}_{:=\bar{\mathbf{g}}_k} + \mathbf{H}\Delta\bar{\mathbf{u}}_k \quad (5.9)$$

where F , G , H and H_d are given in Appendix A, Equations (A.2) - (A.5).

The cost function is

$$J = (\bar{\mathbf{y}}_{k+1} - \bar{\mathbf{r}}_{k+1})^T \mathbf{Q}(\bar{\mathbf{y}}_{k+1} - \bar{\mathbf{r}}_{k+1}) + \Delta\bar{\mathbf{u}}_k^T \mathbf{R}\Delta\bar{\mathbf{u}}_k \quad (5.10)$$

where the weighting matrices $\mathbf{Q} \in \mathbb{R}^{(p \cdot N_p, p \cdot N_p)}$ and $\mathbf{R} \in \mathbb{R}^{(m \cdot N_c, m \cdot N_c)}$ have following properties:

- A required choice is, if both are positive semi-definite.
- Symmetrical matrices.
- Commonly diagonal matrices.

The controller error is defined as

$$\bar{\mathbf{e}}_k = \bar{\mathbf{g}}_k - \bar{\mathbf{r}}_{k+1} \quad (5.11)$$

and when inserting Equation (5.9) and Equation (5.11) into Equation (5.10) the cost function is rewritten as:

$$J = \overline{\Delta\mathbf{u}}_k^T (\mathbf{H}^T \mathbf{Q} \mathbf{H} + \mathbf{R}) \overline{\Delta\mathbf{u}}_k + 2\overline{\Delta\mathbf{u}}_k^T \mathbf{H}^T \mathbf{Q} \bar{\mathbf{e}}_k \quad (5.12)$$

Figure 5.1 shows the block diagram of the considered model predictive control.

5. Model predictive control

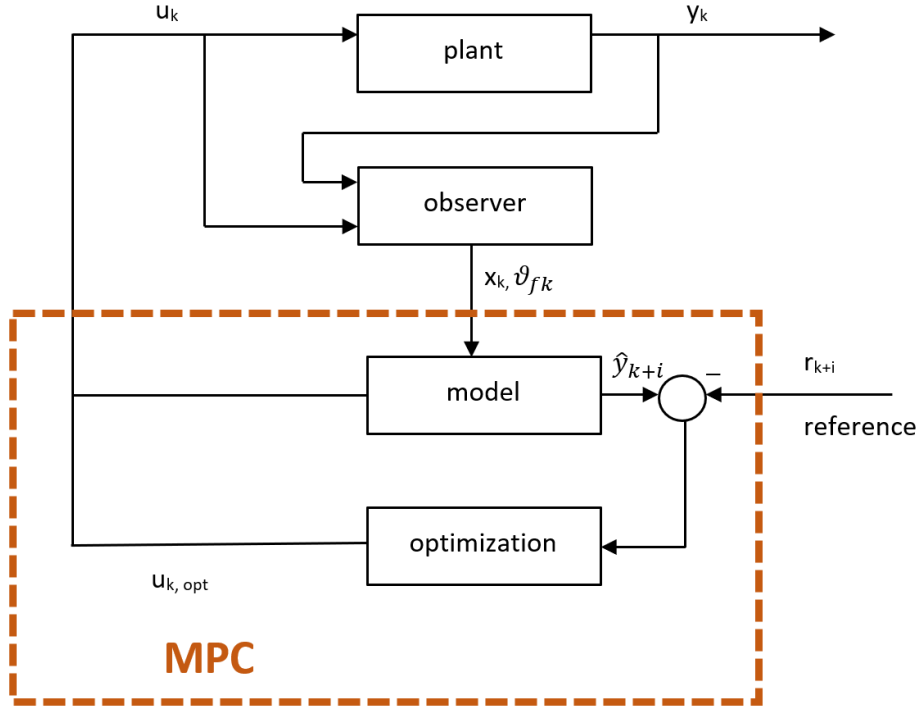


Figure 5.1.: Block diagram of MPC

5.1. Model predictive control without considering constraints

In the unconstrained case the minimum of the cost function is calculated with the partial derivative of Equation (5.12) with $\frac{\partial J}{\partial \Delta \bar{u}_k} = 0$. The actuating variable calculates as

$$\Delta \bar{u}_k = -(\mathbf{H}^T \mathbf{Q} \mathbf{H} + \mathbf{R})^{-1} \mathbf{H}^T \mathbf{Q} \bar{e}_k \quad (5.13)$$

$$\text{where } \mathbf{H}^T \mathbf{Q} \mathbf{H} \succeq 0 \text{ has to be positive semi-definite.} \quad (5.14)$$

Figure 5.2 shows an experiment from MPC algorithm without constraints on the test rig. The parameters are: $T_d = 1s$, A_d was generated with a fixed flow rate $\phi = 500 \text{ ml/min}$, $N_p = 100$, $N_C = 1$, $\mathbf{Q} = 5 \cdot \text{diag}(N_p)$, $R = 2$. The state vector x_k and the temperature ϑ_{r_k} are from the observer represented in Section 4.1. At the experiment at minute 55 the flow rate was reduced manually from $\phi = 500 \frac{\text{ml}}{\text{min}}$ to $\phi = 300 \frac{\text{ml}}{\text{min}}$, because the heater power was not sufficient for the reference value 65°C .

In general, this algorithm has no mechanism to avoid overshoots in the cylinder temperature, so this approach is not further investigated.

5.2. Model predictive control with constraints

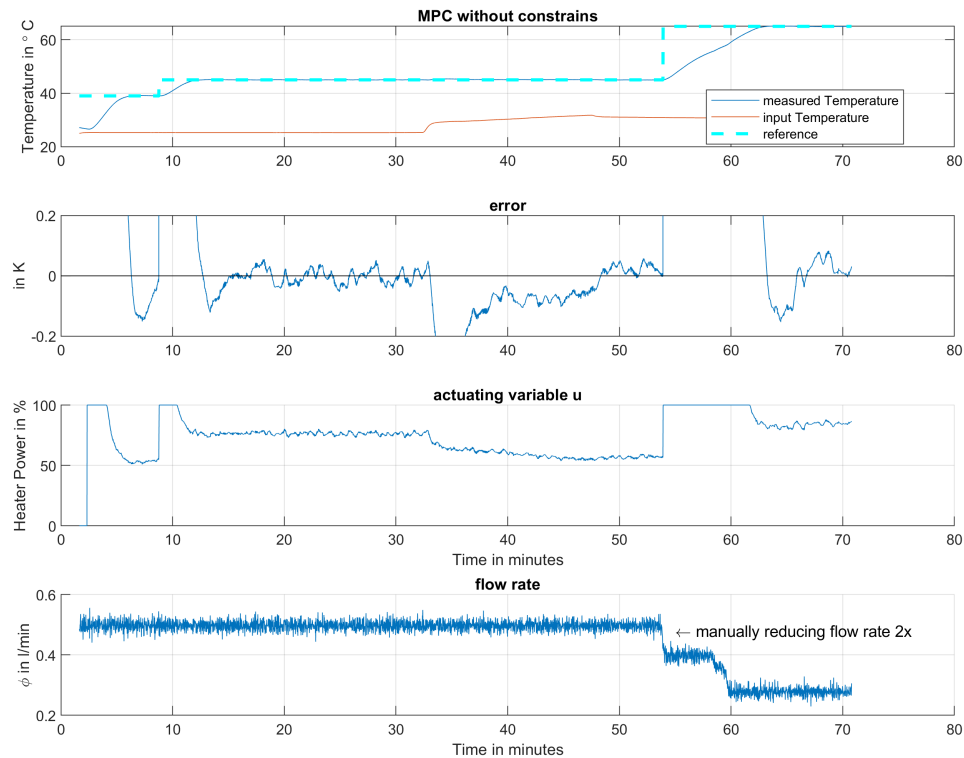


Figure 5.2.: Time diagrams from an experiment of MPC without constraints on the test rig.

5.2. Model predictive control with constraints

A guarantee that the boiling point of isopropanol will not be exceeded is given by the Model predictive controller with constraints.

5.2.1. Theory

The real strength of MPC is the ability to consider constraints. Constraints can be considered for the state variable x_k , the actuating variable u_k , changes to the actuating variable Δu_k and the output variable y_k . For the flow heater, constraints to the actuating variable and to the output variable are used. The constraints to the actuating variable are:

$$u_{min} \leq u_k \leq u_{max} \quad \forall k \geq 0 \quad u_k \in \mathbb{R} \quad (5.15)$$

$$\text{with } u_{min} = 0\% \text{ and } u_{max} = 100\% \quad (5.16)$$

5. Model predictive control

The control algorithm has to take the constraints into account for the entire control horizon, which can be written as

$$\bar{\mathbf{u}}_{min} \leq \mathbf{L}\mathbf{u}_{k-1} + \mathbf{M}\Delta\bar{\mathbf{u}}_k \leq \bar{\mathbf{u}}_{max} \quad (5.17)$$

$$\text{with } \bar{\mathbf{u}}_{min} = \begin{bmatrix} u_{min} \\ u_{min} \\ \vdots \\ u_{min} \end{bmatrix} \quad \text{Dimension : } (m \cdot N_c, 1) \quad (5.18)$$

$$\bar{\mathbf{u}}_{max} = \begin{bmatrix} u_{max} \\ u_{max} \\ \vdots \\ u_{max} \end{bmatrix} \quad \text{Dimension : } (m \cdot N_c, 1) \quad (5.19)$$

$$\mathbf{L} = \begin{bmatrix} \mathbf{E} \\ \mathbf{E} \\ \vdots \\ \mathbf{E} \end{bmatrix} \quad \text{Dimension : } (m \cdot N_c, m) \quad (5.20)$$

$$\text{and } \mathbf{M} = \begin{bmatrix} \mathbf{E} & 0 & \cdots & 0 \\ \mathbf{E} & \mathbf{E} & 0 & \cdots \\ \vdots & & \ddots & 0 \\ \mathbf{E} & \cdots & \cdots & \mathbf{E} \end{bmatrix} \quad \text{Dimension : } (m \cdot N_c, m \cdot N_c) \quad (5.21)$$

Note that for the one-dimensional case $m = 1, N_c = 1$ the scalar 1 is inserted instead of the Unit Matrix \mathbf{E} .

The constraint for the output variable are

$$y_{min} \leq \hat{y}_{k+j} \leq y_{max} \quad \text{with } j = 1, 2, \dots, N_p \quad (5.22)$$

using the predicted output (Equation (5.9)) can be written as

$$\bar{\mathbf{y}}_{min} \leq \bar{\mathbf{g}}_k + \mathbf{H}\Delta\bar{\mathbf{u}}_k + \mathbf{H}_d\bar{\boldsymbol{\vartheta}}_{fk} \leq \bar{\mathbf{y}}_{max} \quad (5.23)$$

with the constraints

$$\bar{\mathbf{y}}_{min} = \begin{bmatrix} y_{min} \\ \vdots \\ y_{min} \end{bmatrix} \quad \text{and} \quad \bar{\mathbf{y}}_{max} = \begin{bmatrix} y_{max} \\ \vdots \\ y_{max} \end{bmatrix} \quad (5.24)$$

The constraints from Equation (5.17) and Equation (5.23) are summarized as

$$\mathbf{W}\Delta\mathbf{u}_k \leq \bar{\mathbf{w}}, \quad \text{where } \bar{\mathbf{w}} = \begin{bmatrix} \mathbf{L}\mathbf{u}_{k-1} - \bar{\mathbf{u}}_{min} \\ \bar{\mathbf{u}}_{max} - \mathbf{L}\mathbf{u}_{k-1} \\ \bar{\mathbf{g}}_k - \bar{\mathbf{y}}_{min} \\ \bar{\mathbf{y}}_{max} - \bar{\mathbf{g}}_k \end{bmatrix} \quad \text{and } \mathbf{W} = \begin{bmatrix} -\mathbf{M} \\ \mathbf{M} \\ -\mathbf{H} \\ \mathbf{H} \end{bmatrix} \quad (5.25)$$

Note that the expression \bar{w} is non-constant and is calculated in every sampling step, whereas W remains constant. The following optimization problem has to be solved in every sampling interval, derived from Equation (5.12):

$$\begin{aligned} \min_{\Delta u_k} \quad & \overline{\Delta u_k}^T (H^T Q H + R) \overline{\Delta u_k} + 2 \overline{\Delta u_k}^T H^T Q \bar{e}_k \\ \text{s.t.} \quad & W \Delta u_k \leq \bar{w} \end{aligned} \tag{5.26}$$

For considering constraints, an optimization-algorithm is helpful. Therefore, two algorithms were evaluated: The first is qpOASES, which is a parametric active-set algorithm for quadratic programming [2]. The other is the so-called Hildreth-algorithm.

The paper [3] concludes, that "the Hildreth algorithm can present a solution in a shorter time than qpOASES." Especially at PLCs where computation power is limited, the Hildreth algorithm is suitable. The PLCs from B&R (used for the test-rig-experiments) can run C and C++ code, and it should be possible to run qpOASES - where the c-source-code is available - on a B&R PLC. The migration of the qpOASES-c-source-code on the PLC is beyond the scope of this work. However, there are other possibilities for optimization and Real-Time-communication when using MATLAB and Simulink with B&R PLC, see [8].

In this thesis, only the Hildreth-Solver was tested on the PLC, because Simulink has the option to directly built and run the available MATLAB code from the Hildreth solver on the CPU.

Figure 5.3 shows the Simulink block diagram of the MPC-Controller with the Hildreth-algorithm.

5.2. Model predictive control with constraints

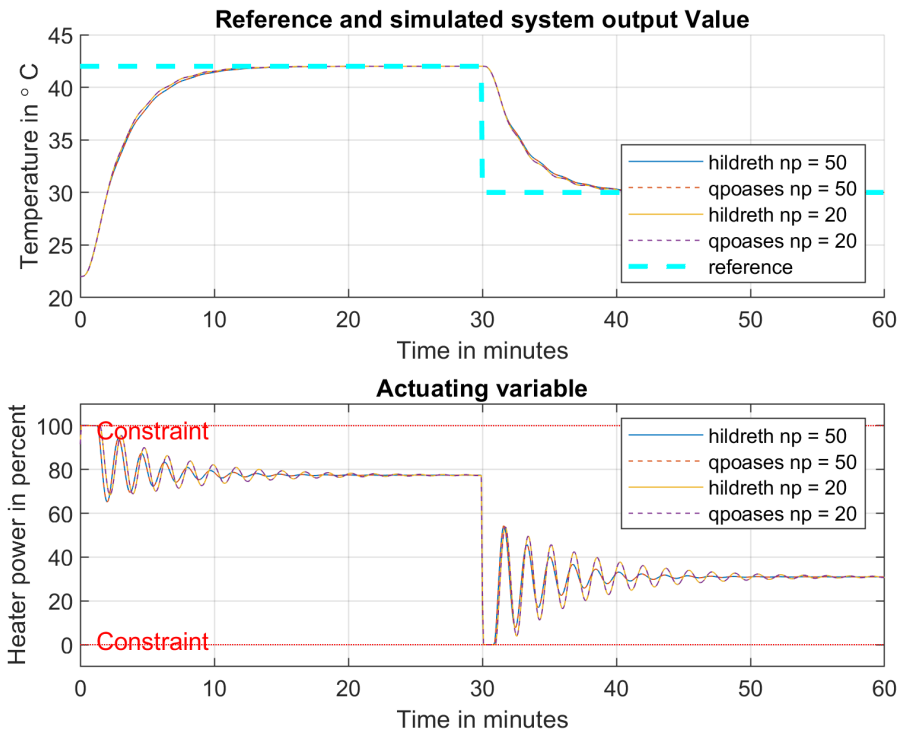


Figure 5.4.: Simulation with constraints to the actuating variable and $T_d = 5s$

5.2.2. Simulation results

The Hildreth algorithm and qpoases are compared with different simulations. Figure 5.4 shows the two algorithms with different prediction horizons. The control horizon $N_c = 5$ and the matrices $Q = 50E$ and $R = E$ and $T_d = 5s$. The simulations in Figure 5.4 are with constraints with respect to the actuating variable. The constraints to the output variable are not active. It can be seen, that the constraints to the actuating variable are met. The actuating variable oscillates, which is caused by the setting $T_d = 5s$. For the next simulations the sampling time was changed to $T_d = 1s$. The settling time for the output variable takes approximately 10 minutes.

5. Model predictive control

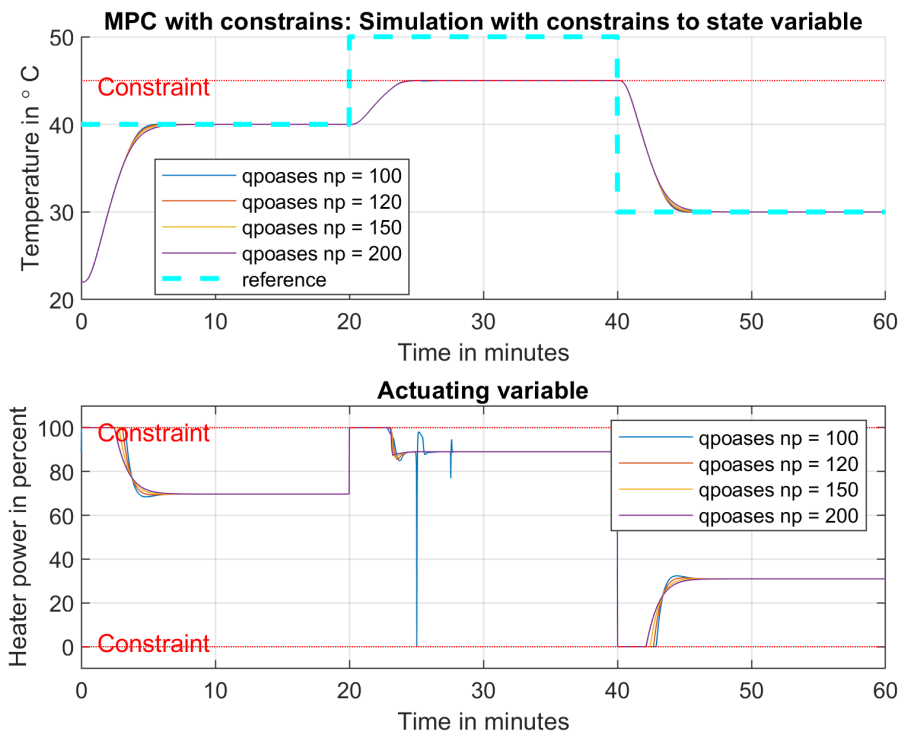


Figure 5.5.: Simulation with constraints, qpoads algorithm with $T_d = 1s$

Figure 5.5 shows simulations with qpoads for different prediction horizons with sampling time $T_d = 1s$. The control horizon was set to $N_c = 2$ and the matrices $Q = 50E$ and $R = E$. The simulation is with constraints to the actuating variable and the constraint to output variable is set to $45^\circ C$. It is shown, that the constraints are met and the settling time is approximately 5 minutes. At minute 25 from the plot of the actuating variable, the algorithm probably predicted a violation of the output constraint and set the actuating variable for a short time to zero. This effect occurs when N_p is chosen too small.

Figure 5.6 shows a simulation result with the qpoads algorithm with the prediction horizon $N_p = 50$ where in the time where the constraint is active (from minute 20 to minute 40) the controller produces oscillations. During the simulation, the ERROR-Message "Premature homotopy termination because QP is infeasible" was often shown in the console. The hildreth algorithm has a similar behaviour when the prediction horizon is chosen too small. Due to this experience, it is recommended that the prediction horizon is at least $N_p = 100$.

5.2. Model predictive control with constraints

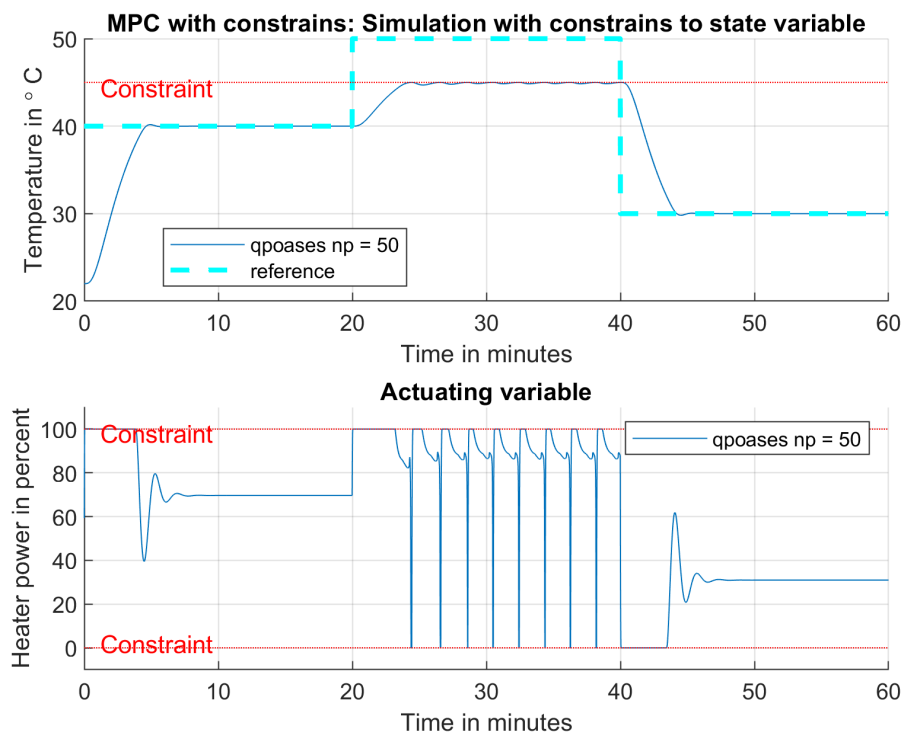


Figure 5.6.: Simulation with constraints qpoases algorithm with $N_p = 50$ and $T_d = 1s$

5. Model predictive control

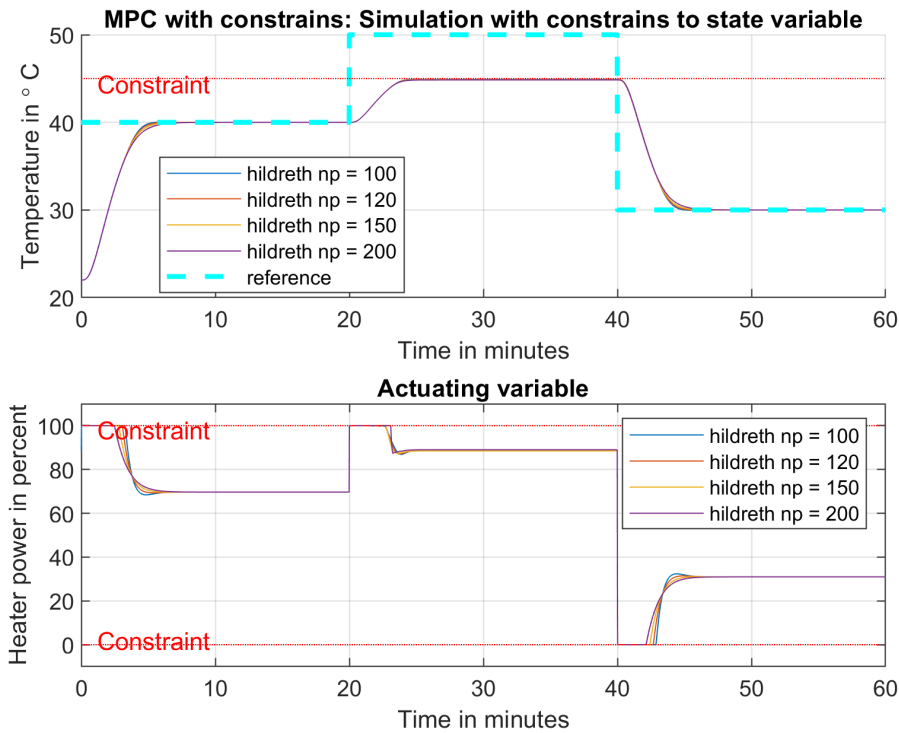


Figure 5.7.: Simulation with constraints Hildereth-algorithm with $T_d = 1s$

Figure 5.7 shows simulations with the Hildreth algorithm for different prediction horizons, where the sampling time $T_d = 1s$. The control horizon was set to $N_c = 2$ and the matrices $Q = 50E$ and $R = E$. The simulation is with constraints to the actuating variable and the constraint to the output variable is set to $45^\circ C$. It is shown, that the constraints are met and the settling time is approximately 5 minutes. The greater the prediction horizon, the earlier the actuating variable starts to change. Concerning the settling time are only slightly differences. The smaller the prediction horizon the shorter the settling time.

A comparison of the results from the Hildreth algorithm and qpooases is given in Figure 5.8 for prediction horizon $N_p = 120$. The control horizon is set to $N_c = 2$ and the matrices $Q = 50E$ and $R = E$. The simulation is with constraints to the actuating variable and the constraint to the output variable is set to $45^\circ C$. The zoomed plot 5.9 shows, that the Hildreth-algorithm in combination with the state observer does not exactly regulate the output variable to it's desired value. There is a margin of approximately $0.12^\circ C$.

5.2. Model predictive control with constraints

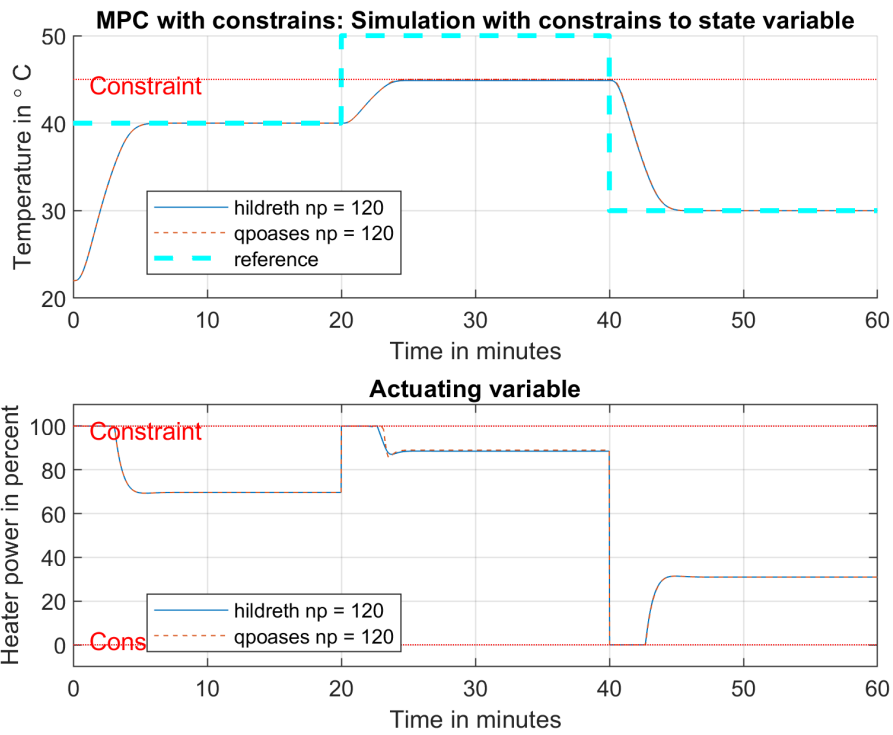


Figure 5.8.: Simulation with constraints, comparison of algorithms with $T_d = 1s$

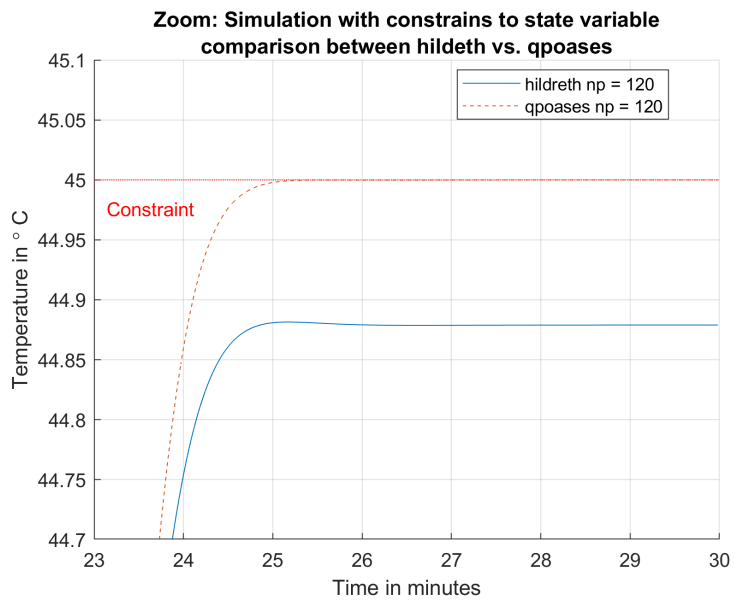


Figure 5.9.: Simulation with constraints, comparison of algorithms with $T_d = 1s$, zoomed view

5. Model predictive control

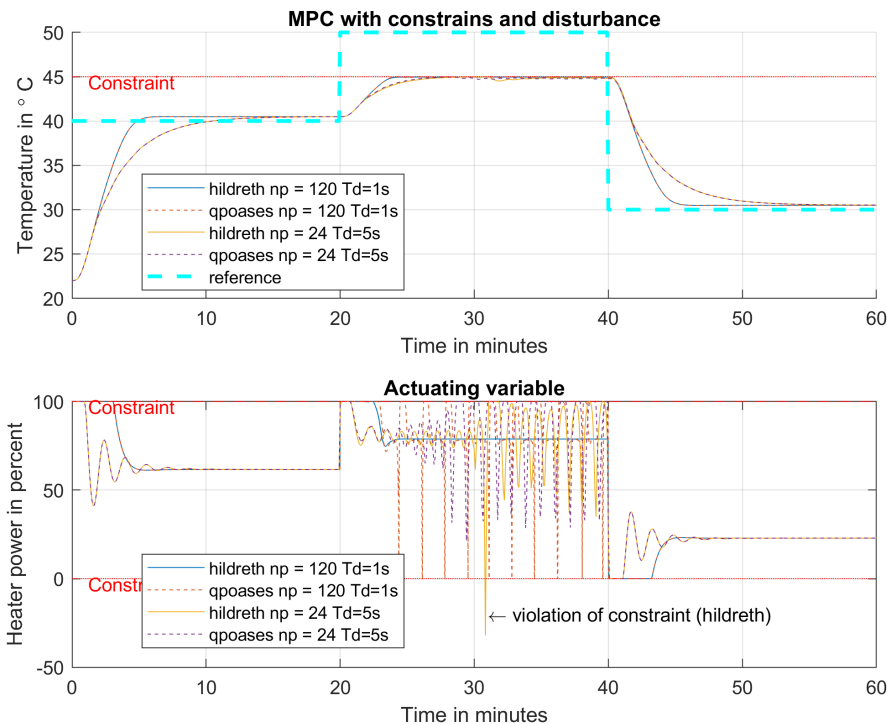


Figure 5.10.: Simulation with constraints and disturbance.

In the next simulations, the algorithms are simulated with constraints and with disturbance. The disturbance is modeled with adding 10 % to the actuating variable directly at the controller output. The plant model and the observer model are fed by 10 % higher actuating variable. The plant model and the observer model are designed with an input saturation. So the disturbance gets active when the actuating variable is lower than 100 %. Figure 5.10 shows the test sequence response from both algorithms. A zoomed plot is given in Figure 5.11. The control horizon was set to $N_c = 2$ and the matrices $Q = 50E$ and $R = E$. The simulation is with constraints to the actuating variable and the constraint to the output variable is set to 45 °C.

A violation of the constraints from the Hildreth-algorithm is marked in Figure 5.10. It is noteworthy that only the basic variant of the Hildreth-algorithm was implemented. There is no function for checking the validity of the optimization result. Whenever using the Hildreth algorithm, there has to be a test for checking the validity of the results, which was considered in this thesis. The only thing that was modeled was an input saturation.

5.2. Model predictive control with constraints

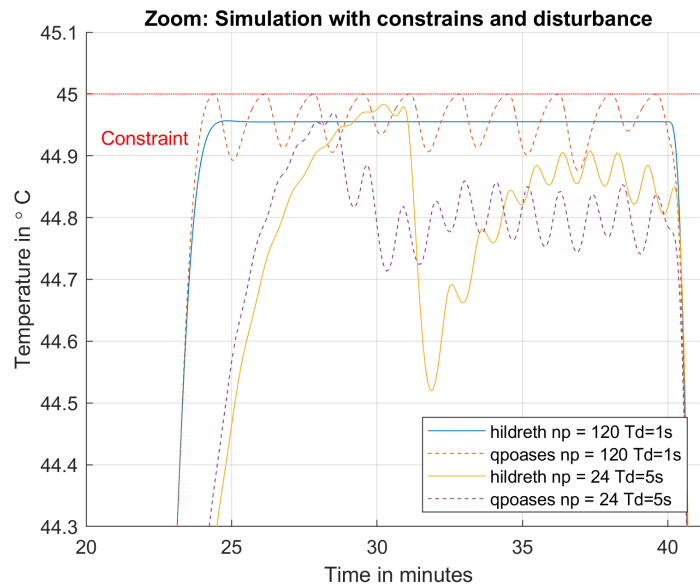


Figure 5.11.: Simulation with constraints and disturbance, zoomed view.

	Constraint	Reference value	Difference
Figure	°C	°C	°C
5.12	40.0	39.9	0.1
5.13	40.0	39.6	0.4
5.14	40.0	39.5	0.5

Table 5.1.: Overview of experiments with MPC with constraints on the test rig

5.2.3. Experimental results

The controller was also tested on the test rig. As mentioned before the experiments on the test rig are with the Hildreth-algorithm. Since the Hildreth-algorithm has the behaviour that there is a margin between constraint and output variable, the reference value was set lower than the constraint. The Table 5.1 gives an overview of the plots from the experiments. The settings are $N_p = 20$, $N_c = 1$, $T_d = 5s$, $Q = 20E$, $R = 1$ with MPC with constraints on the test rig.

In Figure 5.12 the constraint and the reference value are too close. The real system's fluctuation lets the controller for two times leaving the stationary state (At minute 21 and minute 26).

In Figure 5.13 an experiment, where the difference between constraint and reference is 0.4 °C, is shown. The output variable is, after the settling time of approximately 5 minutes, in the ± 0.1 °C - range of the reference value.

The plot in Figure 5.14 is with 0.5 °C difference where the output variable slightly

5. Model predictive control

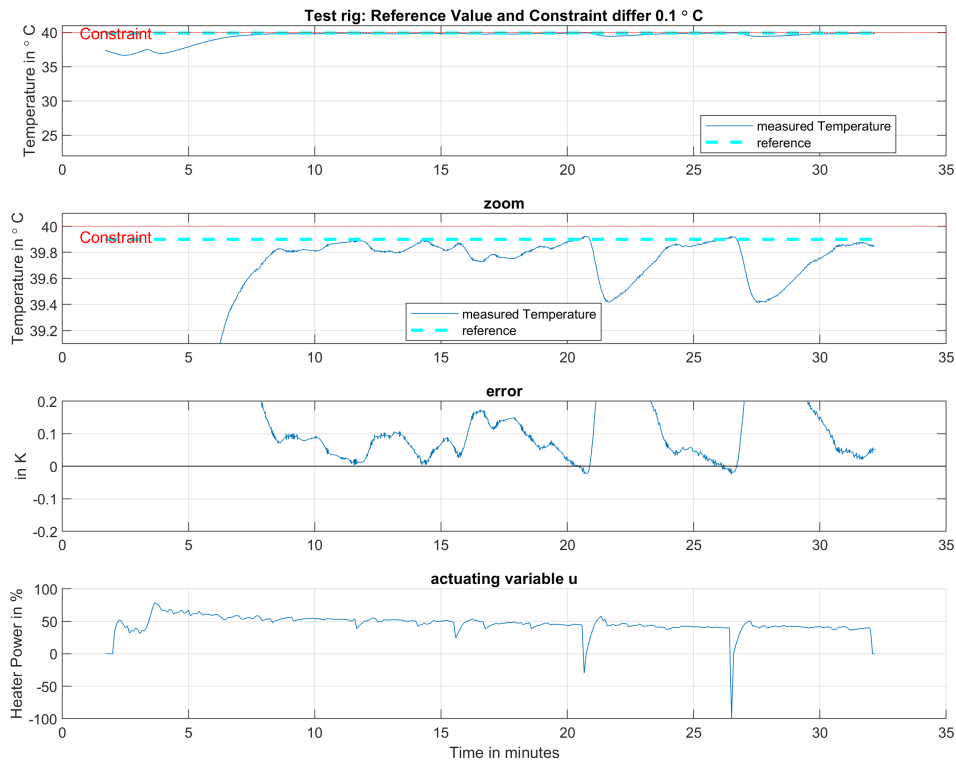


Figure 5.12.: MPC with constraints on the test rig. Difference = 0.1 °C

overshoots at minute eight.

The settling time at the experiments is between 5-7 minutes. The tests were done with one water tank, which heats up during time, so a forecast with linear increasing fluid temperature for the prediction horizon was implemented.

5.3. Results and Comparison

A comparison of the MPC with the state feedback controller is given in Figure 5.15. The model predictive controller yields a shorter settling time and shows less fluctuations.

5.3. Results and Comparison

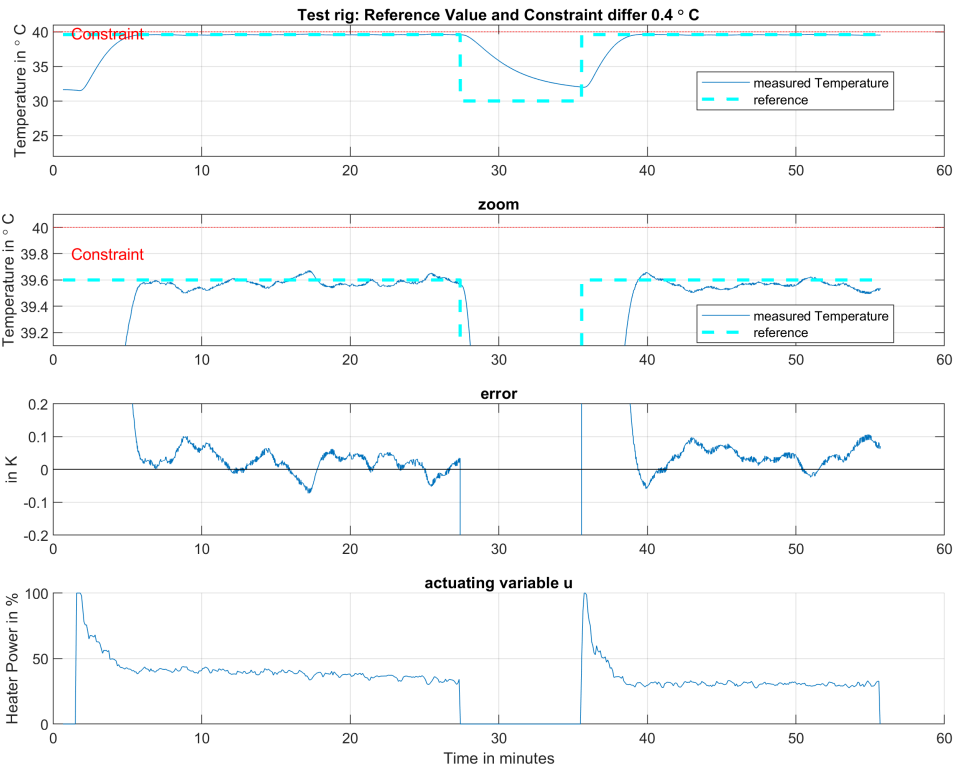


Figure 5.13.: MPC with constraints on the test rig. Difference = 0.4 °C

5. Model predictive control

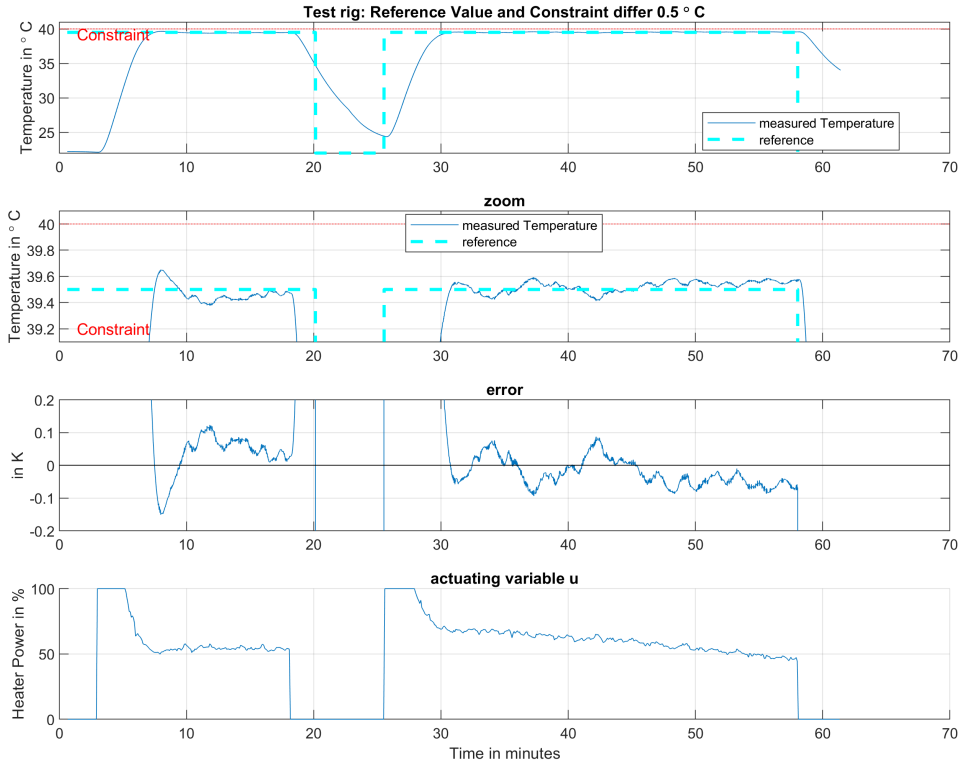


Figure 5.14.: MPC with constraints on the test rig. Difference = 0.5 °C

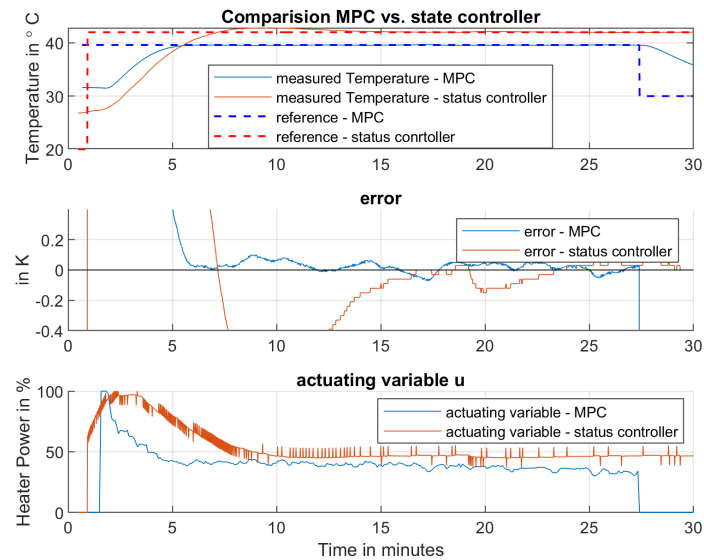


Figure 5.15.: Comparison: MPC vs. Status controller

6. Conclusion

In this master thesis, two different model-based control-algorithms for a flow heater, which is used in the semiconductor industry, have been proposed. The main issue, when controlling flow heaters is their dead-time which, in combination with PI-controllers often leads to poor closed-loop performance such as overshooting.

The proposed state feedback controller and the proposed model-predictive controller are designed based on a mathematical model. Both control methods turned out suitable for the considered plant and outperform a PI control scheme.

A test rig was set up for controller validation, with the flow heater actuated by a pulse-width modulated solid-state relay. The used PLC was a B&R X20 System with the environment MATLAB/Simulink and the Automation Studio Target for Simulink.

The experiments performed within this work show a comparison of the state feedback controller with the model-predictive controller. The model predictive controller yields a shorter settling time and shows less fluctuations. The opportunity to consider constraints in the model predictive controller can be used to avoid overheating of the liquid. Two different solvers were simulated for the model-predictive controller: The Hildreth-solver and the qpooases-solver. The results with the qpooases-solver were flawless; The Hildreth-solver (basic implementation) showed some weaknesses, such as violation of constraints.

Further tasks can be the extension of the Hildreth-solver with a routine that allows checking the validity of the solution, or another task might be the migration of the qpooases-solver in the PLC of the test rig.

Bibliography

- [1] S Farshid Chini and A Amirfazli. Understanding pattern collapse in photolithography process due to capillary forces. *Langmuir*, 26(16):13707–13714, 2010.
- [2] Hans Joachim Ferreau, Christian Kirches, Andreas Potschka, Hans Georg Bock, and Moritz Diehl. qpOASES: A parametric active-set algorithm for quadratic programming. *Mathematical Programming Computation*, 6(4):327–363, 2014.
- [3] B. Huyck, L. Callebaut, F. Logist, H. J. Ferreau, M. Diehl, J. De Brabanter, J. Van Impe, and B. De Moor. Implementation and experimental validation of classic MPC on programmable logic controllers. In *2012 20th Mediterranean Conference on Control Automation (MED)*, pages 679–684, 2012.
- [4] Martin Kleindienst. Design of a model-based liquid flow controller. Alpen-Adria-Universität Klagenfurt, Austria, February 2013.
- [5] Martin Kleindienst, Stefan Koch, and Markus Reichhartinger. Model-based temperature control of a continuous flow heater for efficient processing of silicon wafers. In *2020 IEEE Conference on Control Technology and Applications (CCTA)*, pages 1–6. IEEE, 2020.
- [6] Martin Kleindienst, Markus Reichhartinger, Martin Horn, and Felix Staudegger. Observer-based temperature control of an LED heated silicon wafer. *Journal of Process Control*, 70:96–108, 2018.
- [7] David Q. Mayne. Model predictive control: Recent developments and future promise. *Automatica*, 50(12):2967 – 2986, 2014.
- [8] PETR Pivonka and VOJTECH Miksanek. Real-time communication between matlab/simulink and plc via process visualization interface. In *Actas de 11th WSEAS International Conference on SYSTEMS*, pages 28–32, 2007.
- [9] S.Joe Qin and Thomas A. Badgwell. A survey of industrial model predictive control technology. *Control Engineering Practice*, 11(7):733 – 764, 2003.
- [10] Toshihiko Tanaka, Mitsuaki Morigami, and Nobufumi Atoda. Mechanism of resist pattern collapse during development process. *Japanese Journal of Applied Physics*, 32(Part 1, No. 12B):6059–6064, dec 1993.

Bibliography

- [11] Prof. Fedro S. Zazueta. Surface tension. https://fsz.ifas.ufl.edu/surfacetensionandcapillarity/html/en_tension.htm. (Accessed on 12-09-2020).

Appendix A.

Table of material properties and Equations

Selected materials
Unit-System: SI-Units.

μ ... thermal conductivity
 ρ ... material's specific density
 c ... material's specific heat capacity

Material	c in $\frac{J}{kgK}$	μ in $\frac{W}{mK}$	ρ in $\frac{kg}{m^3}$
Aluminium	900	210	2700
PFA Flourpolymer (Material the tubes are made)	960	0,24	2120
Water	4200	0,556	997
Isopropanol	2700	0,173	786

$$\kappa_{Aluminium} = \frac{\mu}{\rho c} = \frac{236 \frac{W}{mK}}{2700 \frac{kg}{m^3} \cdot 900 \frac{J}{kgK}} = \frac{97.12 \cdot 10^{-6} \frac{m^2}{s}}{s} \quad (A.1)$$

Appendix A. Table of material properties and Equations

Equations for Chapter 5:

$$\mathbf{F} = \begin{bmatrix} \mathbf{c}_d^T \mathbf{A}_d \\ \mathbf{c}_d^T \mathbf{A}_d^2 \\ \vdots \\ \mathbf{c}_d^T \mathbf{A}_d^{N_p} \end{bmatrix} \quad \text{Dimension } (p \cdot N_p, n) \quad (\text{A.2})$$

$$\mathbf{G} = \begin{bmatrix} \mathbf{c}_d^T \mathbf{b}_d \\ \mathbf{c}_d^T \cdot (\mathbf{A}_d + \mathbf{E}) \cdot \mathbf{b}_d \\ \mathbf{c}_d^T \cdot (\mathbf{A}_d^2 + \mathbf{A}_d + \mathbf{E}) \cdot \mathbf{b}_d \\ \vdots \\ \mathbf{c}_d^T \cdot (\mathbf{A}_d^{N_p-1} + \dots + \mathbf{A}_d + \mathbf{E}) \cdot \mathbf{b}_d \end{bmatrix} \quad \text{Dimension } (p \cdot N_p, m) \quad (\text{A.3})$$

$$\mathbf{H}_d = \begin{bmatrix} \mathbf{c}_d^T \mathbf{f}_d & 0 & \dots & 0 \\ \mathbf{c}_d^T \cdot \mathbf{A}_d \cdot \mathbf{f}_d & \mathbf{c}_d^T \mathbf{f}_d & 0 & \vdots \\ \vdots & \ddots & \ddots & \\ \mathbf{c}_d^T \cdot \mathbf{A}_d^{N_p-1} \cdot \mathbf{f}_d & \dots & \dots & \mathbf{c}_d^T \mathbf{f}_d \end{bmatrix} \quad \text{Dimension } (p \cdot N_p, p \cdot N_p) \quad (\text{A.4})$$

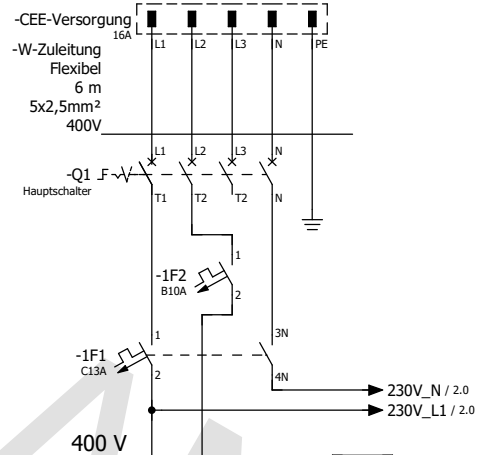
$$\mathbf{H} = \begin{bmatrix}
\mathbf{c}_d^T \mathbf{b}_d & 0 & \cdots & 0 \\
\mathbf{c}_d^T \cdot (\mathbf{A}_d + \mathbf{E}) \cdot \mathbf{b}_d & \mathbf{c}_d^T \mathbf{b}_d & \cdots & 0 \\
\vdots & \vdots & \ddots & \vdots \\
\mathbf{c}_d^T \cdot (\mathbf{A}_d^{N_c-1} + \cdots + \mathbf{A}_d + \mathbf{E}) \cdot \mathbf{b}_d & \mathbf{c}_d^T \cdot (\mathbf{A}_d^{N_c-1} + \cdots + \mathbf{A}_d + \mathbf{E}) \cdot \mathbf{b}_d & \cdots & \mathbf{c}_d^T \mathbf{b}_d \\
\mathbf{c}_d^T \cdot (\mathbf{A}_d^{N_c} + \cdots + \mathbf{A}_d + \mathbf{E}) \cdot \mathbf{b}_d & \mathbf{c}_d^T \cdot (\mathbf{A}_d^{N_c} + \cdots + \mathbf{A}_d + \mathbf{E}) \cdot \mathbf{b}_d & \cdots & \mathbf{c}_d^T \cdot (\mathbf{A}_d + \mathbf{E}) \cdot \mathbf{b}_d \\
\vdots & \vdots & \vdots & \vdots \\
\mathbf{c}_d^T \cdot (\mathbf{A}_d^{N_p-1} + \cdots + \mathbf{A}_d + \mathbf{E}) \cdot \mathbf{b}_d & \mathbf{c}_d^T \cdot (\mathbf{A}_d^{N_p-1} + \cdots + \mathbf{A}_d + \mathbf{E}) \cdot \mathbf{b}_d & \cdots & \mathbf{c}_d^T \cdot (\mathbf{A}_d^{N_p-N_c} + \cdots + \mathbf{A}_d + \mathbf{E}) \cdot \mathbf{b}_d
\end{bmatrix} \tag{A.5}$$

Dimension $(p \cdot N_p, m \cdot N_c)$

Appendix B.

Schematic

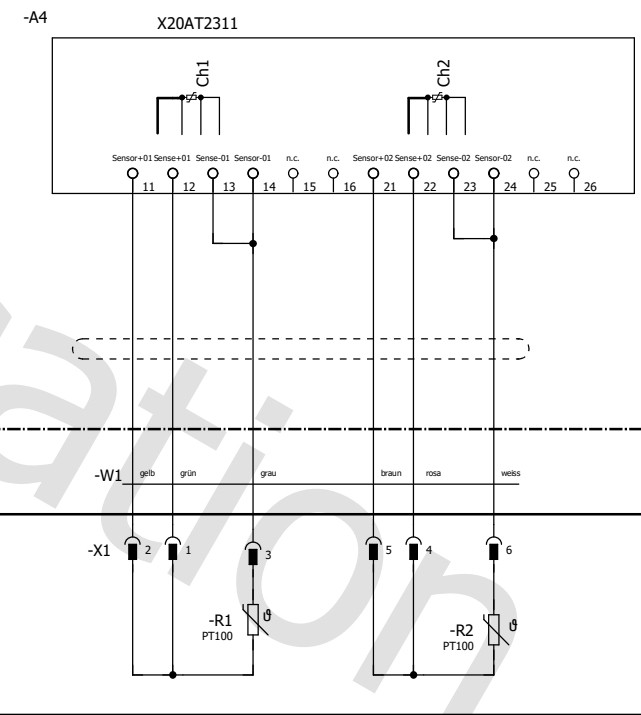
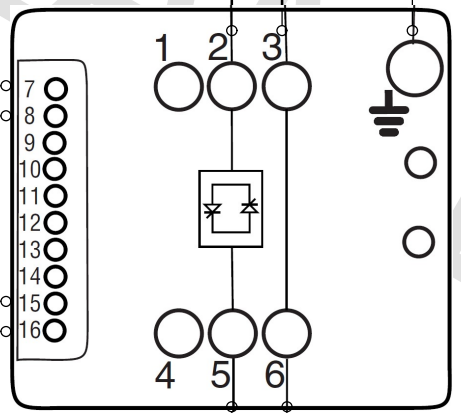
Zuleitung: 16 A, CEE, 5-polig
Kabellänge: 6m



Schaltplan vom Teststand Lam Research Durchlauferhitzer

Masterarbeit: Modellbildung Simulation und Reglerentwurf eines Durchlauferhitzers
Matthias Wahrbichler, ab Juli 2019

Analogausgang 4-20 mA von der SPS
AQ+01I / 8.3
AO-01 / 8.3

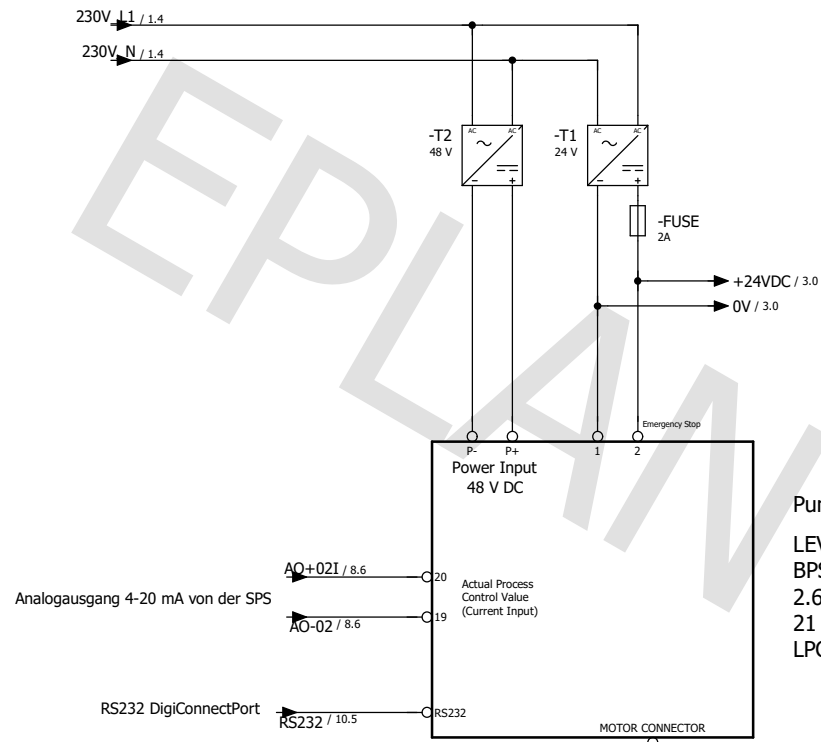


Ohmscher Widerstand:
165 Ohm bei 20°C
165 Ohm bei 45°C

PROCESS TECHNOLOGY, USA
1400 Watt
480V 2,9A
900/1400 = 64 %
400 V 2,3 A 900 W

Heizer mit Temperatursensoren

		Datum	29.03.2020	EPLAN	IRT TU Graz	Spannungsversorgung und Heizer	=
		Bearb.	LAPTOP-HP				+
		Gepr		gemäß IEC-Norm: Seitenstruktur mit Anlage und Einbaort			
Änderung	Datum	Name	Urspr	Ersatz von	Ersetzt durch		Blatt 1 Seite 1 / 10



LEVITRONIX
BPS-200
LPC-200.3 Controller
Firmware C2.88 R07 Specification

Digital In1, (Signal)	2	<i>Emergency Stop</i>	24 V	⇒	not active
Ground Digital In1	1		0 V	⇒	active
Analog In2, (Signal)	20	<i>Actual Process Control Value</i>	4..20 mA = 0..100%		
Ground Analog In2	19				

Pump Controller
LEVITRONIX
BPS-200
2.6 bar
21 liters/min
LPC-200.3 Controller

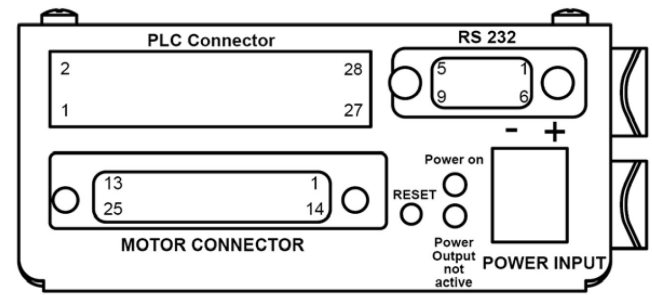
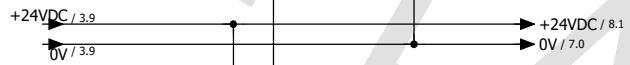
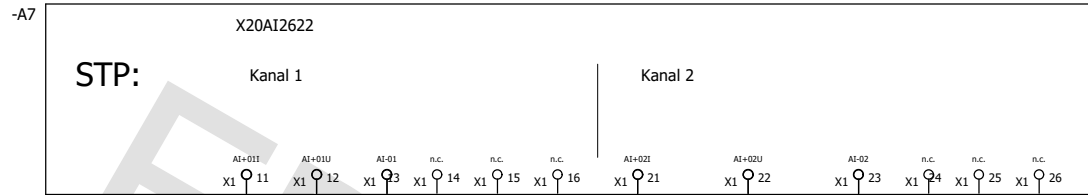


Figure 3: Front View of LPC-200.3 (Extension Board PLC/RS232)



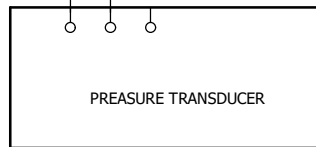
Einschalten der Pumpe mit der LEVITRONIX Service Software vom PC



+extern

-W-P1.2

red black

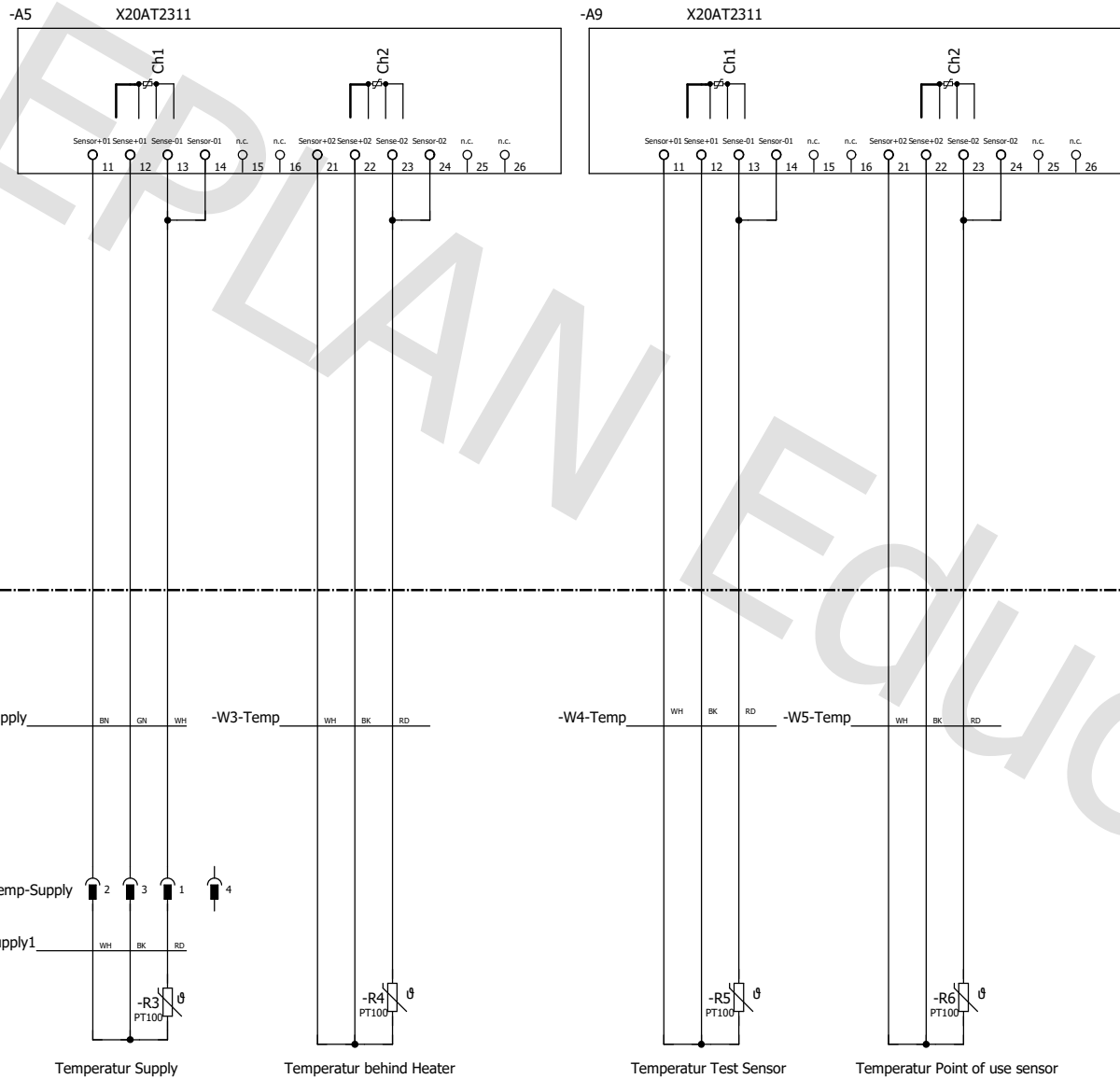


Pressure P1.2

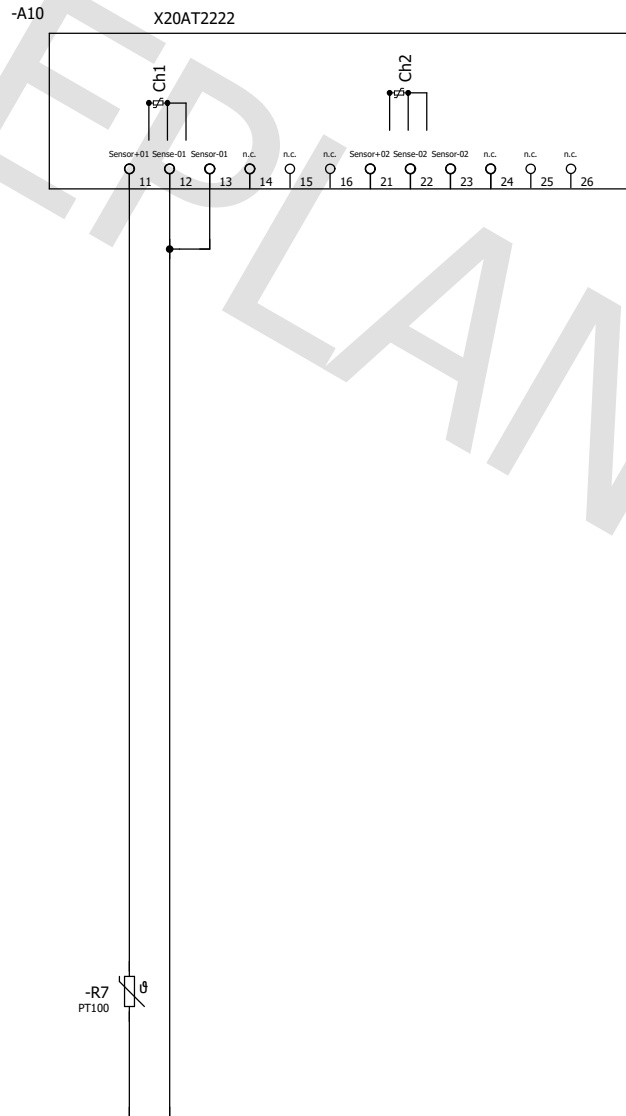
3

5

			Datum	29.03.2020	EPLAN	IRT TU Graz	Analogeingänge 2	=
			Bearb.	LAPTOP-HP				+
			Gepr		gemäß IEC-Norm: Seitenstruktur mit Anlage und Einbaort			
Änderung	Datum	Name	Urspr		Ersatz von	Ersetzt durch		
							IEC_tpl001	Blatt 4 Seite 4 / 10



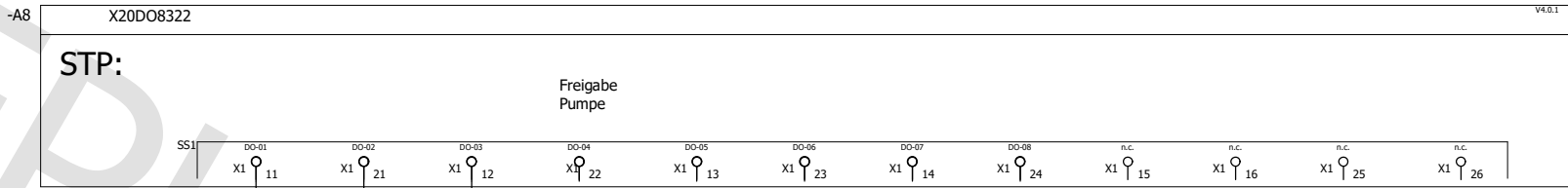
		Datum 29.03.2020		EPLAN		IRT TU Graz		Flüssigkeitstemperatursensoren		=	
		Bearb. LAPTOP-HP								+	
		Gepr		gemäß IEC-Norm: Seitenstruktur mit Anlage und Einbaort							
Änderung		Datum		Name		Urspr		Ersatz von		Ersetzt durch	
								IEC_tpl001		Blatt 5 Seite 5 / 10	



Temperatursensor am Metallzylinder. Ca. 1.4 cm außerhalb des Zentrums.

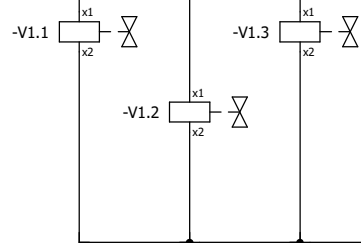
5				Datum 29.03.2020	EPLAN	IRT TU Graz	Heizer-Kern-Temperatursensor	=	
			Bearb. LAPTOP-HP	gemäß IEC-Norm: Seitenstruktur mit Anlage und Einbauort				+	
			Gepr			IEC_tpl001	Blatt 6		
Änderung	Datum	Name	Urspr	Ersatz von	Ersetzt durch			Seite 6 / 10	

Kanäle aufzählend

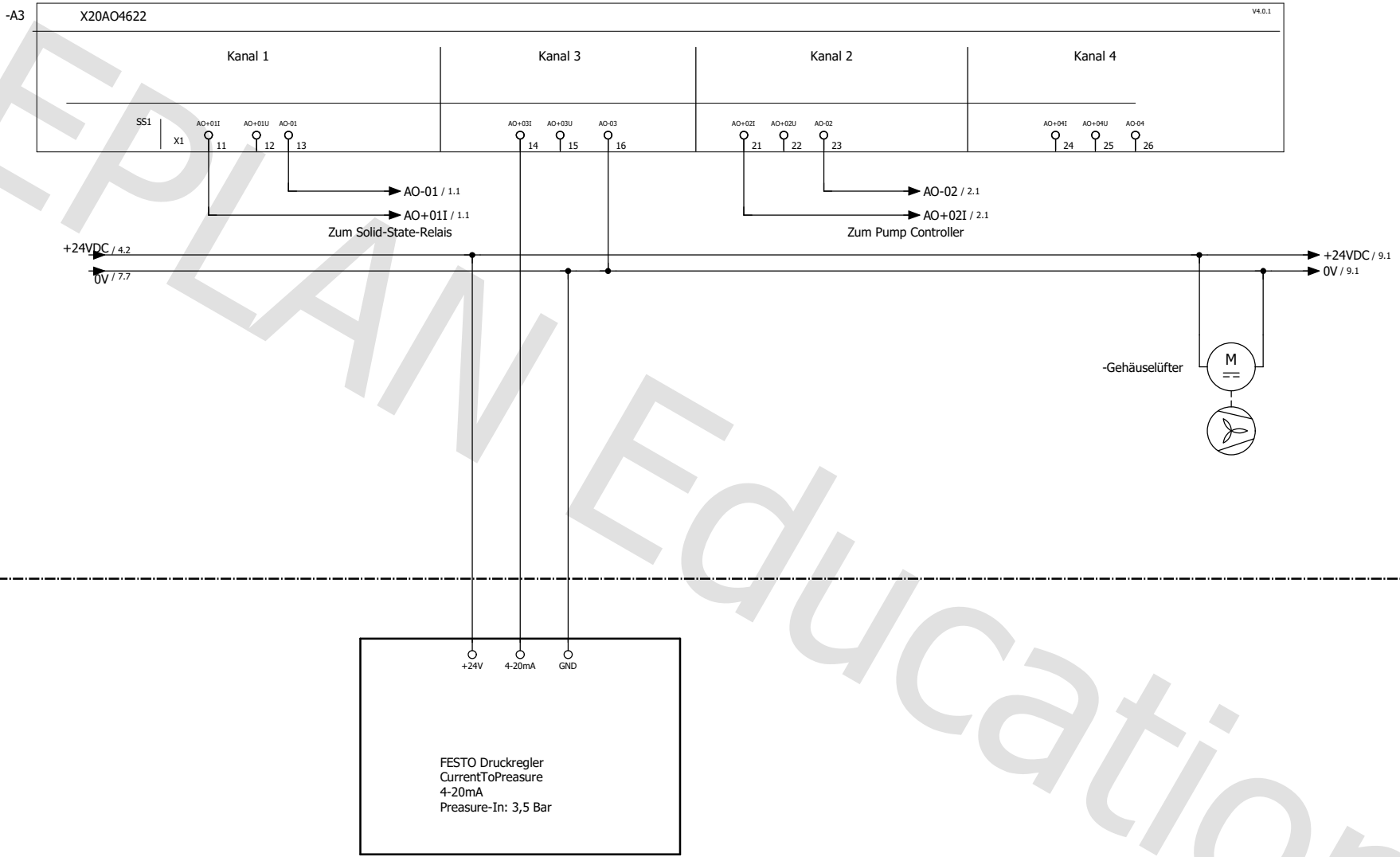


+extern

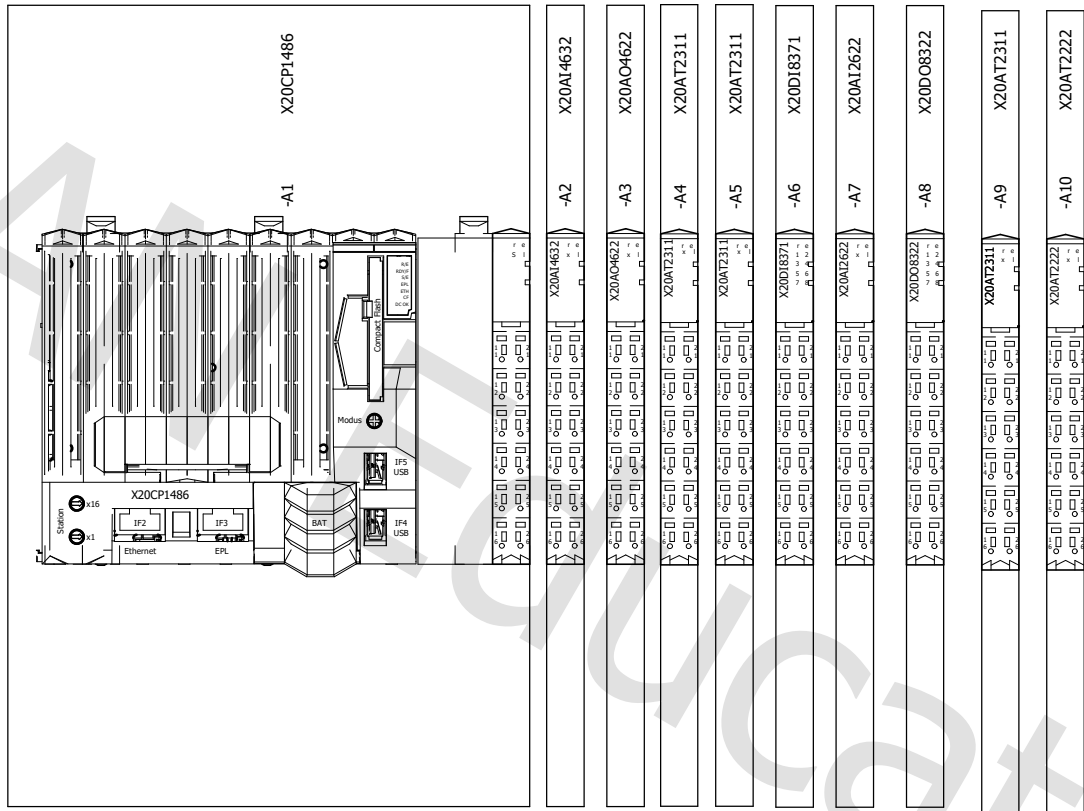
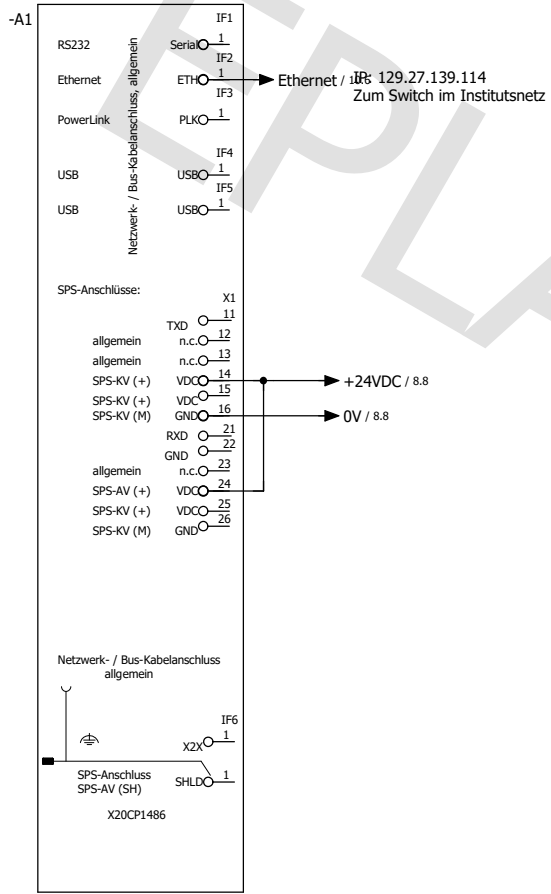
-W-Ventile



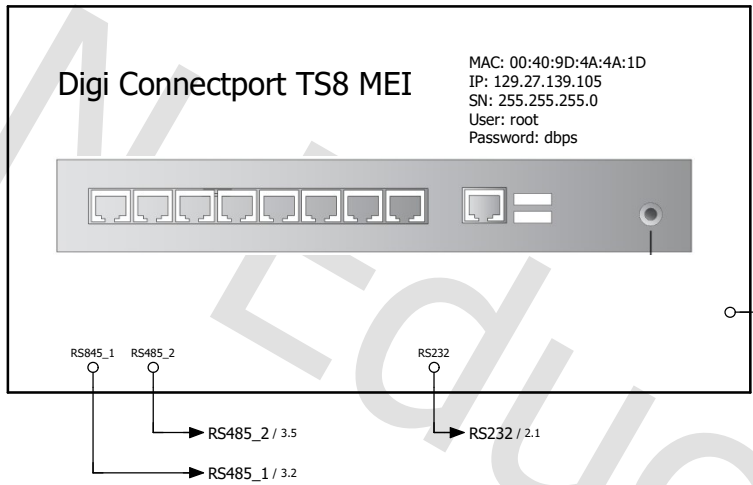
			Datum	29.03.2020	EPLAN	IRT TU Graz	Digitalausgänge	=
			Bearb.	LAPTOP-HP				+
			Gepr		gemäß IEC-Norm: Seitenstruktur mit Anlage und Einbaort			
Änderung	Datum	Name	Ürspr		Ersatz von	Ersetzt durch		
							IEC_tpl001	Blatt 7 Seite 7 / 10



+extern



			Datum 29.03.2020	EPLAN	IRT TU Graz	SPS_Gesamt	=
			Bearb. LAPTOP-HP				+
			Gepr.	gemäß IEC-Norm: Seitenstruktur mit Anlage und Einbaort			
Änderung	Datum	Name	Urspr	Ersatz von	Ersetzt durch		
						IEC_tpl001	Blatt 9 Seite 9 / 10



○ → Ethernet / 9.1 IP: 129.27.139.105
 Zum Switch im Institutsnetz

			Datum	29.03.2020	EPLAN	IRT TU Graz	DigiConnectport	=
			Bearb.	LAPTOP-HP				+
			Gepr		gemäß IEC-Norm: Seitenstruktur mit Anlage und Einbaort			
Änderung	Datum	Name	Urspr		Ersatz von	Ersetzt durch		IEC_tpl001
								Blatt 10 Seite 10 / 10